EES Catalysis

REVIEW ARTICLE

View Article Online
View Journal | View Issue

Cite this: *EES Catal.*, 2025, 3, 921

Non-TiO_2-based photoanodes for photoelectrocatalytic wastewater treatment: electrode synthesis, evaluation, and characterization†

Jingyang Liu,[abc] Huizhong Wu,[abc] Jiangli Sun,[abc] Shuaishuai Li,[abc] Aydin Hassani [de] and Minghua Zhou *[abc]

To address the increasingly serious problem of water pollution, photoelectrocatalysis (PEC), one of the advanced oxidation processes (AOPs), has gained significant attention due to its ability to utilize sunlight and its low energy consumption. In PECs, TiO_2 is the most widely used and established photoanode; however, non-TiO_2-based photoanodes have increasingly become a focus for improving visible light utilization and meeting the requirements of specific reactions. The performance of these non-TiO_2-based photoanodes in wastewater treatment varies based on different synthesis strategies and structures. Therefore, this paper critically reviews the synthesis, evaluation and characterization methods of non-TiO_2-based photoanodes used in wastewater treatment. Specifically, it reveals the application potential of various non-TiO_2-based photoanodes (such as WO_3, ZnO, g-C_3N_4, and $BiVO_4$), compares the costs and electrode stability of different synthesis methods from a practical application-oriented perspective, elucidates the synthesis–structure–mechanism–activity relationship, proposes an evaluation framework for PEC wastewater treatment based on multiple dimensions (including pollutant removal, electrode stability, light utilization efficiency, and environmental applicability), and introduces frontier theoretical simulations and characterization techniques of PEC wastewater treatment in depth according to the reaction process. Finally, an outlook on the preparation, evaluation and characterization of non-TiO_2-based photoanodes is proposed, covering perspectives from the atomic level to large-scale applications. This work aims to provide a comprehensive understanding of these 'rising stars' and guide the synthesis of photoanodes with enhanced performance, as well as more accurate evaluation and characterization.

Received 8th March 2025,
Accepted 28th May 2025

DOI: 10.1039/d5ey00068h

rsc.li/eescatalysis

Broader context

Photocatalysis is an innovative technique for addressing energy and environmental challenges, leveraging sunlight to generate green energy and facilitate the removal of pollutants. Nevertheless, conventional photocatalytic processes utilizing powdered semiconductors encounter significant limitations, such as the recombination of photogenerated charges and challenges in recycling, which impede their practical applications. In contrast, photoelectrocatalysis (PEC), which integrates photocatalysis with an externally applied electric field, presents a promising strategy to these challenges and has garnered considerable attention in the fields of energy production and pollutant remediation. Although TiO_2 remains the most extensively studied photocatalyst, recent advancements have led to the development of non-TiO_2-based photoanodes, which exhibit substantial potential for PEC wastewater treatment. This review summarizes progress in non-TiO_2-based photoanodes, comparing their stability and cost across preparation strategies. It summarizes the evaluation frameworks for photoelectrodes in wastewater treatment and provides novel insights. Furthermore, it introduces characterization techniques for each PEC step and analyzes the synthesis–structure–mechanism–activity relationship. Finally, prospects, challenges, and opportunities from atomic to large-scale synthesis and characterization are discussed. By providing a comprehensive understanding of these materials, this review aims to guide the synthesis of photoelectrodes for environmental applications and enhance the mechanistic understanding of PEC processes.

[a] *Key Laboratory of Pollution Process and Environmental Criteria, Ministry of Education, College of Environmental Science and Engineering, Nankai University, Tianjin 300350, China. E-mail: zhoumh@nankai.edu.cn*
[b] *Tianjin Key Laboratory of Environmental Technology for Complex Trans-Media Pollution, College of Environmental Science and Engineering, Nankai University, Tianjin 300350, China*
[c] *Tianjin Advanced Water Treatment Technology International Joint Research Center, College of Environmental Science and Engineering, Nankai University, Tianjin 300350, China*
[d] *Department of Materials Science and Nanotechnology Engineering, Faculty of Engineering, Near East University, 99138 Nicosia, TRNC, Mersin 10, Turkey*
[e] *Research Center for Science, Technology and Engineering (BILTEM), Near East University, 99138 Nicosia, TRNC, Mersin 10, Turkey*

† Electronic supplementary information (ESI) available. See DOI: https://doi.org/10.1039/d5ey00068h

1. Introduction

Water pollution is closely related to human health and is one of the most concerning issues in the world. To tackle this issue, more and more wastewater treatment techniques have been used. However, when treating recalcitrant organics, biotechnology is limited and needs a large area to operate[1,2] while physical methods can't completely remove pollutants, causing secondary pollution.[3] Advanced oxidation processes (AOPs) can efficiently remove pollutants and even mineralize them, showing promising application potential.[4,5] AOPs include ultraviolet (UV)-based technologies,[6] O_3-based technologies,[7] Fenton process,[8] electrochemical advanced oxidation processes (EAOPs),[9] photocatalysis (PC) process[10,11] *etc.*, among which photocatalysis can work under sunlight, showing promise for solving environmental problems and alleviating energy stress at the same time. However, there are still many problems in PC, which limit its practical applications. For instance, photo-generated holes (h^+) and electrons (e^-) are easy to combine, thus decreasing the quantum yield of photocatalysts.[12] What's more, photocatalysts are usually dispersed in solution, and they are difficult to separate from treated water.[13]

To improve charge carriers' separation efficiency and reusability, photoelectrocatalysis (PEC), the combination of PC and electrocatalysis (EC), is proposed. The photocatalysts are immobilized on conductive substrates; thus, the prepared photoelectrode can be easily cycled, and e^-–h^+ pairs are more likely to separate after applying an electric field.[14] Compared with photocathodes, photoanodes are more popularly used in wastewater treatment because h^+ accumulating at their surface can oxidize organic pollutants directly or indirectly.[15] Fig. 1 illustrates literature statistics on photoanodes since 2000. In Fig. 1a, it can be seen that TiO_2-based photoanodes have been the most studied photoanodes since the beginning of this century. However, the research proportion of non-TiO_2-based photoanodes has increased in recent years, which has increased from less than 20% before 2015 to more than half recently. On the one hand, non-TiO_2-based photocatalysts have different band positions compared with TiO_2, which can meet the requirements of different reactions. For example, $BiVO_4$, WO_3, and their

Jingyang Liu

Jingyang Liu is currently a PhD candidate at Nankai University under the supervision of Prof. Minghua Zhou. He earned his BSc degree in Environmental Engineering from the Hebei University of Technology in 2022 and subsequently enrolled in a combined Master-PhD program at Nankai University the same year. His research focuses on photoelectrocatalytic wastewater treatment technologies and the detoxification of industrial wastewater.

Huizhong Wu

Huizhong Wu is currently a PhD candidate under the supervision of Prof. Minghua Zhou in the College of Environmental Science and Engineering at Nankai University and a visiting PhD in the University of Barcelona. Her current research primarily focuses on the design of photoanodes and their applications in renewable energy technologies.

Jiangli Sun

Jiangli Sun is a PhD candidate under the supervision of Prof. Minghua Zhou at the College of Environmental Science and Engineering at Nankai University. Her research interests mainly focus on wastewater treatment and resource recycling by using photoelectrocatalytic technology.

Shuaishuai Li

Shuaishuai Li is currently pursuing his PhD degree under the supervision of Professor Minghua Zhou at the College of Environmental Science and Engineering at Nankai University. He obtained his BSc degree in Chemical Engineering and Technology from the Taiyuan Institute of Technology in 2017. His current research focuses on the rational design and sustainable synthesis of novel functional nanomaterials, with particular emphasis on their application in advanced wastewater treatment and resource recovery systems.

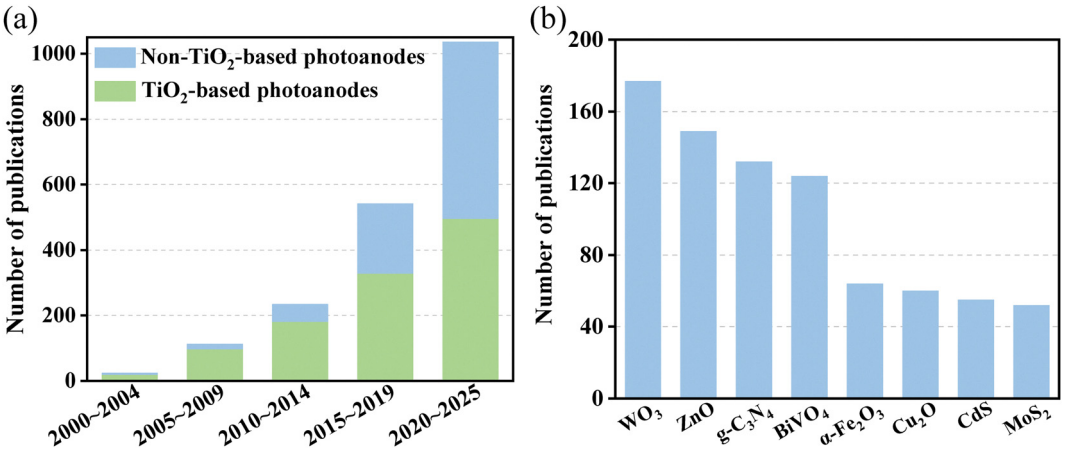

Fig. 1 Bibliometric study on photoanodes used for wastewater treatment: (a) comparison of the number of publications between TiO_2-based photoanodes and non-TiO_2-based photoanodes in different periods. (b) Comparison of the number of publications between eight main non-TiO_2-based photoanodes. Data from 2000 to April 2025, according to the Web of Science database. Keywords: (wastewater OR pollutant) AND (photoanode OR photoelectrocatalysis OR photoelectrocatalytic) NOT ("water oxidation" OR "water splitting").

composites are more suitable as photoanodes in the PEC–chlorine (PEC–Cl) system.[16] On the other hand, many non-TiO_2-based photoanodes offer unique advantages. For example, g-C_3N_4 is a metal-free polymer that exhibits visible-light-driven photocatalytic activity and high stability.[17] It shows significant potential in future clean energy production and environmental compatibility. In the field of wastewater treatment, the eight most prominent non-TiO_2-based photoanodes are shown in Fig. 1b, with WO_3, ZnO, g-C_3N_4, and $BiVO_4$ leading the way.

The preparation methods of these photoanodes are also different; some catalysts (WO_3, $BiVO_4$, *etc.*) can directly grow on substrates, while some photoanodes (g-C_3N_4, for example) have to be prepared by *ex situ* methods. Some synthesis methods are operated at room temperature and atmospheric pressure (*e.g.*, successive ionic layer adsorption and reaction (SILAR)[18]), while some require special equipment, even high temperature and pressure (*e.g.*, hydrothermal method[19]). Different synthesis strategies result in electrodes with different structures and hence different activities, so synthesis methods need to be summarized and compared. However, in previous reviews,[20,21] synthesis methods of photoanodes are briefly introduced (*e.g.*, their operations, advantages, and disadvantages), while the comparison of products (pollutant removal efficiency, stability, cost, *etc.*) is not conducted, and the synthesis–activity relationship is not revealed.

Moreover, to reveal the structure–activity relationship, light–matter interaction, and photocatalyst–pollutant interaction, sufficient evaluation and characterization should be carried out. The mechanism of PEC processes needs to be deeply understood. However, in previous reviews,[21–24] when discussing characterization techniques, they are usually divided into characterization of morphology (scanning electron microscopy (SEM), transmission electron microscopy (TEM), *etc.*), chemical composition (X-ray photoelectron spectroscopy (XPS), X-ray diffraction (XRD) spectra, *etc.*), and photoelectric properties (photoluminescence (PL) spectroscopy, UV/vis diffuse

Aydin Hassani

Aydin Hassani received his PhD in Physical Chemistry from Atatürk University, Turkey, in 2016. Following his doctoral studies, he worked as a postdoctoral researcher at Atatürk University for one year. Between April and July 2014, he was a Visiting Researcher at the University of Bologna in Italy. In 2017, he joined the Department of Materials Science and Nanotechnology Engineering at Near East University, Cyprus as an Assistant Professor and was promoted to Associate Professor in 2020. His research focuses on developing nanostructured and functionalized nanomaterials for energy and environmental applications.

Minghua Zhou

Minghua Zhou is currently a distinguished professor and associate Dean at the College of Environmental Science and Engineering at Nankai University. He obtained his BSc (1998) and PhD (2003) from the Department of Environmental Engineering at Zhejiang University. After his postdoctoral research at the University of Sydney, he joined Nankai University in 2008. He is a Fellow of the Royal Society of Chemistry and ranked among Most Cited Chinese Researchers (Environmental Science) by Elsevier since 2014. His research focuses on advanced oxidation processes for wastewater remediation, environmental catalysis and functional nanomaterials, and sustainable water reuse technologies.

reflectance spectroscopy (UV-vis DRS), *etc.*). The relationship between the photoanodes and pollutant removal has not been thoroughly summarized. What's more, in recent years, *in situ* XPS, *in situ* infrared, density functional theory (DFT) calculation, computational fluid dynamics (CFD) simulation, *etc.* have gradually emerged to characterize the morphology, composition, and reaction mechanism of non-TiO_2-based photoanodes. Therefore, an in-depth summary of existing and latest characterization techniques is needed.

Herein, this review compares and concludes the synthesis methods, evaluation systems, and characterization techniques of non-TiO_2-based photoanodes for wastewater treatment. First, the fundamentals of PEC wastewater treatment are explained, and based on an analysis of the literature, the application trends of non-TiO_2-based photoanodes are presented. Subsequently, the main synthesis methods for non-TiO_2-based photoanodes are summarized and compared. Next, the evaluation of PEC wastewater treatment at the practical application level is presented, and the main techniques for characterizing non-TiO_2-based photoanodes are described in depth from the PEC reaction process. Finally, an outlook on the preparation, evaluation, and characterization of non-TiO_2-based photoanodes is proposed based on the perspective from the atomic level to large-scale applications. This review innovatively summarizes the impact of electrode synthesis on electrode structure and performance, systematically compares diverse synthesis strategies from the perspectives of product stability and cost-effectiveness, and highlights cutting-edge experimental and theoretical approaches for characterizing PEC wastewater treatment processes. We hope this review will inspire interested readers in the synthesis of superior photoanodes for wastewater treatment and in-depth characterization of them.

2. Fundamentals of PEC wastewater treatment

The PEC wastewater treatment process can be divided into three steps: light absorption and exciton excitation, separation and transport of carriers, and interface reaction.[10] The relationship between the three steps is shown in Scheme 1. Due to the difference between the Fermi energy level of the photoanode and the redox potential of the solution, electron transfer occurs at the interface between the semiconductor and the solution, forming an energy band bending and space charge layer (SCL) on the surface.[25] In step one, when the energy of absorbed light is higher than the bandgap energy (E_g), e^- in the valence band (VB) transit to the conduction band (CB), causing h^+ to be left in the VB.[14] In this step, the e^- and h^+ generated in the bulk phase, if not effectively separated, will quickly recombine[26] (as demonstrated by the dashed arrows in Scheme 1, including bulk-phase recombination, SCL recombination, and surface-state recombination), and can't participate in the pollutant degradation reaction. In the second step, the simultaneous presence of light and anode bias leads to a more pronounced energy band bending, which favors the separation of photogenerated carriers.[25] Within the SCL, h^+ move towards the

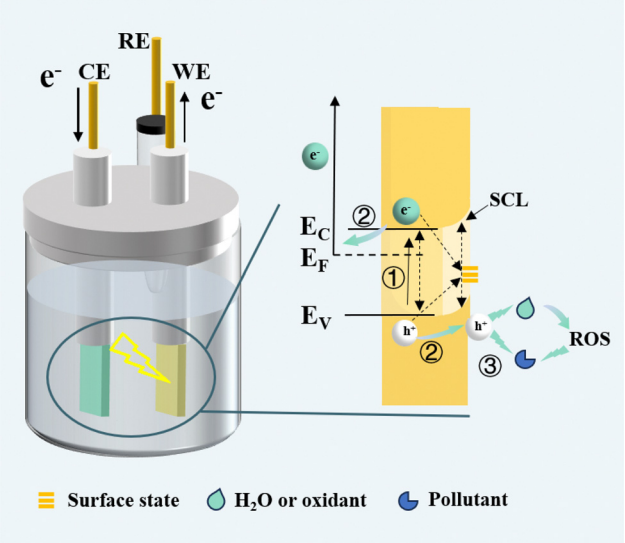

Scheme 1 Schematic diagram of the process around the photoanode for PEC wastewater treatment (n-type semiconductor as an example). CE: counter electrode, RE: reference electrode, WE: working electrode, E_C: conduction band potential, E_F: Fermi energy level, E_V: valence band potential, SCL: space charge layer, ROS: reactive oxygen species.

electrode surface, while e^- migrate to the cathode *via* an external circuit. In the interfacial reaction in the third step, the accumulated h^+ may oxidize the contaminant directly, or they may oxidize water or other oxidants to generate reactive species with strong oxidizing properties.[16] The type of oxidation reaction that occurs depends on the catalyst's CB and VB potentials, the electrode bias, and the mass transfer of the contaminant. Throughout the process, the lifetimes of electrons and holes in the bulk phase are only picoseconds to nanoseconds, whereas the reactions to degrade pollutants are on the timescale of milliseconds to seconds, suggesting that the kinetics of carriers within the photoanode are very critical.[27] The selection of photoanode materials and different synthesis methods may affect carrier migration and redox reaction kinetics, which in turn affect the pollutant removal efficiency. Therefore, a summary of photoanode synthesis methods and characterization of the PEC process is essential for understanding and breaking through the barriers to pollutant degradation kinetics.

3. Application trend of non-TiO_2 based photoanodes in PEC water treatment

The energy band structures of the eight most common non-TiO_2-based photoanodes are shown in Fig. 2a, in which MoS_2 and Cu_2O are p-type semiconductors and the others are n-type semiconductors. Metrological analysis of the retrieved literature reveals the research hotspots and trends of non-TiO_2-based photoanodes in the field of wastewater treatment. The results show that compared with TiO_2-based photoanodes, the two most obvious application trends in non-TiO_2 photoanodes are as follows: one is that the proportion of the literature with "fuel

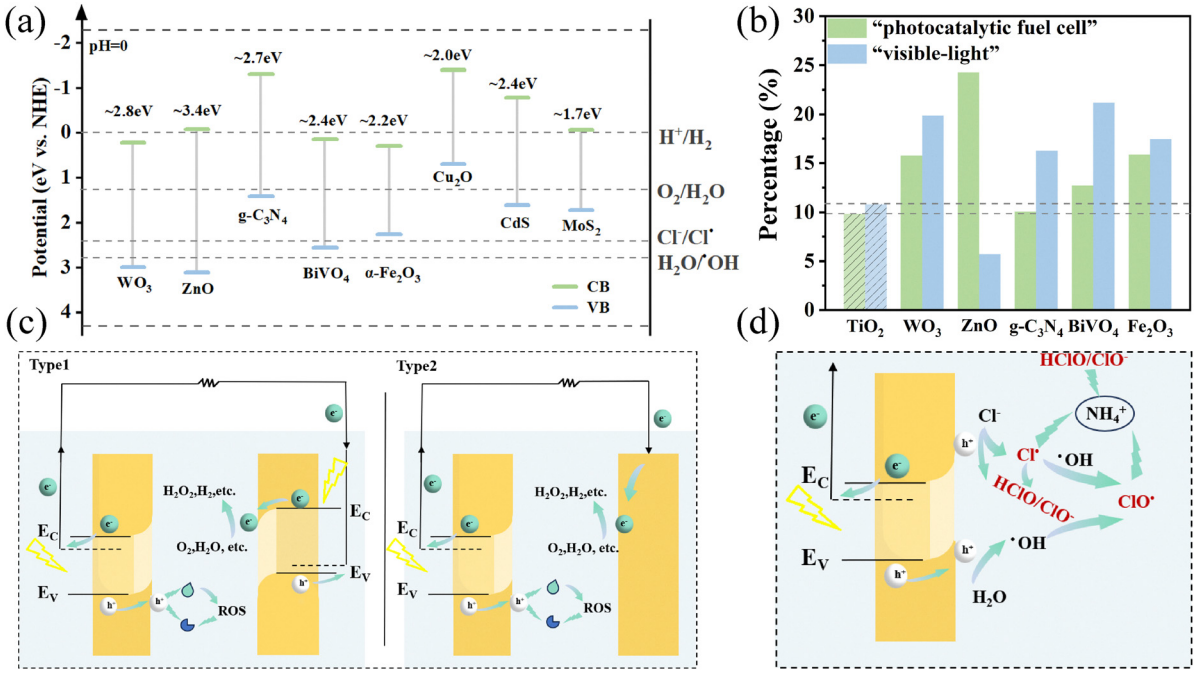

Fig. 2 (a) The band structures of eight main non-TiO_2-based photoanodes. Data from ref. 33–36. (b) Bibliometric analysis of TiO_2 and the five most frequently used non-TiO_2-based photoanodes. (Counting the keywords in the titles of the literature, filtering out words like 'and', 'of', 'degradation', and 'photoanode' that do not reflect the key information, and the most significant remaining keywords are "fuel cell", "visible-light", and the proportion of the literature containing these keywords to the total literature was calculated.) (c) The schematic of two types of PFCs with non-TiO_2-based photoanodes. (d) A schematic diagram of the possible sources of RCS generation in the PEC–Cl system.[34]

cell" and "electricity" as keywords is higher than that with TiO_2, which is represented by ZnO and WO_3; another is that the proportion of "visible-light" as the keyword is also significantly higher than that with TiO_2 as the keyword, represented by WO_3, g-C_3N_4, $BiVO_4$, and α-Fe_2O_3.

A photocatalytic fuel cell (PFC) is a special PEC water treatment system. The non-TiO_2-based photoanode can be combined with a photocathode (type 1) or a cathode without light response (type 2) to form a PFC (Fig. 2c). It relies on the photovoltage generated by the photoelectrode after illumination to drive the reaction without external bias.[28] The theoretical maximum value of the photovoltage between the two electrodes depends on the Fermi energy level difference between the electrodes, so it is necessary to select the appropriate anode and cathode.[29] In the photoanode–photocathode system, under light illumination, the photoanode undergoes energy band bending (upward) near the surface of the solution, and e^- migrate towards the cathode, while h^+ accumulate on the surface of the photoanode, and oxidation reactions take place.[30] The photocathode undergoes downward energy band bending, which facilitates the aggregation of electrons towards the cathode for reduction reactions to occur at its surface. Contaminants can be oxidized at the anode, and electrons gathered at the cathode may undergo a variety of reduction reactions, depending on the electrode material and the redox potential. Wang *et al.*[31] used oxygen vacancy-rich $BiVO_4$ as a photoanode, Pt/C cocatalyst-coated Si as a photocathode, and the pollutant triethanolamine as "fuel" to construct a PFC system for the simultaneous degradation of pollutants and hydrogen production, which can achieve bias-free H_2 production with a current density of 10.17 mA cm^{-2}. Dong *et al.*[32] constructed an artificial leaf with simultaneous H_2O_2 production at the cathode and anode using SnO_{2-x}/$BiVO_4$/WO_3 as a photoanode and Mo-SACs/mrG as a cathode without the need for applied voltage, achieving an unassisted H_2O_2 production rate of 0.77 μmol (min^{-1} cm^{-2}) under 1 sun AM 1.5 illumination. The most obvious advantage of a PFC is that it can generate electricity while degrading pollutants, making it a promising technology to address the environmental and energy crisis.

One of the key issues in PEC wastewater treatment is the use of light, with only 5% of sunlight being the most energetic UV light and 43% being visible light.[10] Semiconductors possessing too high a bandgap energy can only utilize UV light, as can be seen in Fig. 2a, where all photoanode materials except ZnO have smaller bandgap energies compared with TiO_2 (~3.2 eV). This is why all photoanodes except for TiO_2 and ZnO have been reported in such a high percentage of visible-light studies. However, most of the current studies on "visible light PECs" use simulated sunlight, and the use of actual sunlight for pollutant degradation needs to be taken seriously. Sun *et al.*[37] studied a MgO/g-C_3N_4 S-scheme heterojunction photoanode, which showed superior visible light utilization prospects. This anode was combined with modified carbon felt to construct a new PEC system. In the actual PEC degradation experiment under sunlight, 98.12% of tetracycline was removed within 30 min. Xie *et al.*[38] synthesized a $BiVO_4$-decorated WO_3 photoanode, which was combined with an electrodeposited polyaniline-decorated carbon fiber

cathode to construct a solar-driven wastewater resuscitation system. The system was operated under natural sunlight and achieved 99.1% uranium reduction and 98.4% oxytetracycline hydrochloride removal, showing superior practical application potential.

It is noteworthy that for non-TiO_2-based photoanodes, the keyword ''ammonia'' also appears more frequently in WO_3 and $BiVO_4$ due to the increasing application of PEC–Cl systems in the treatment of ammonia-containing wastewater. The active chlorine species (RCS) have obvious advantages over $^{\bullet}OH$ in the treatment of NH_3–N,[39] so the core of PEC–Cl is the formation of RCS (Fig. 2d). The selection of photoanode materials is extremely critical in controlling the generation of RCS and inhibiting the generation of toxic chlorine-containing by-products. The valence band potential of some photoanodes (*e.g.*, Fe_2O_3 and g-C_3N_4) is not sufficient to oxidize Cl^-, and therefore, they are not suitable as photoanode materials (see Fig. 2a). Some photoanodes have too large a bandgap and require UV excitation (*e.g.*, ZnO), which are also not suitable as photoanode materials. Therefore, $BiVO_4$, WO_3, and their composites are most often considered for PEC–Cl.[34] It has also been shown by some researchers that too much oxidizing capacity of the valence band generates more $^{\bullet}OH$, which is detrimental to the generation of RCS. For example, Zhang *et al.*[16] reported a self-driven PEC–Cl system with a $BiVO_4/WO_3$ heterojunction photoanode. In order to control toxic chlorate and nitrate caused by the excessive oxidation capacity of $^{\bullet}OH$, they realized the predominant production of $Cl^{\bullet}$ by regulating the valence band edge of WO_3 through modifying $BiVO_4$. The results showed that 10 mg L^{-1} ammonia-N was completely removed in 120 min, and toxic byproducts chlorate and nitrate were inhibited by 79.3% and 31%, respectively, compared to the WO_3 photoanode. The PEC–Cl system has also demonstrated potential in addressing combined organic–inorganic contamination. For instance, Zhang *et al.*[40] fabricated a novel $WO_3/BiVO_4$-CoBi photoanode, which could remove 99% of carbamazepine (CBZ) within 40 min and 75.4% of NH_4^+ within 120 min.

4. Synthesis of non-TiO_2-based photoanodes

The synthesis of photoanodes differs significantly from that of powder photocatalysts, necessitating careful consideration of substrate selection and growth methodology employed. Synthesis techniques encompass wet-chemical methods, electrochemical methods, other chemical methods, and physical methods. Based on whether photocatalysts are directly grown on substrates or whether pre-prepared powder photocatalysts are affixed to them, synthesis methods can be classified into *in situ* and *ex situ* categories. A summary of several *in situ* synthesis methods for non-TiO_2-based photoanodes utilized in wastewater treatment is presented in Table 1 and Fig. 3.

4.1 Wet-chemical methods

Wet-chemical methods are the most popular and facile methods for the preparation of non-TiO_2-based photoanodes. The sol–gel method is a very popular wet chemistry method for the preparation of TiO_2-based photoanodes;[21] however, this method is not commonly used for the preparation of non-TiO_2-based photoanodes. Hydrothermal methods can grow catalysts on conductive substrates in a Teflon-lined stainless-steel autoclave at high temperature and pressure; it is always followed by annealing (Fig. 4a). Solvothermal methods use organic solvents as the reaction medium[41] and are also conducted in autoclaves; however, this approach has limited applications. Similar to the hydrothermal method, chemical bath deposition (CBD) grows films by heating the precursor and substrate, but it doesn't require an enclosed space and high pressure, and it is sometimes referred to as the dip-coating method. Liquid phase deposition (LPD), based on the ligand-exchange hydrolysis of the metal-fluoro complex and the F^- consumption reaction of boric acid,[42] is another wet-chemical method. CBD and LPD are ''softer'' in conditions because they don't require high pressure and temperature (Fig. 4b). SILAR is conducted by alternately immersing the substrate in different anionic and cationic solutions for many cycles (Fig. 4c). Ratnayake *et al.*[43] deposited a $BiVO_4$ thin film on FTO using the SILAR method, and they studied the effect of deposition parameters, including precursor concentration, number of immersion cycles, and annealing temperature, on the properties and PEC efficiency of the $BiVO_4$ photoanode. Instead of immersing the substrate in the solution directly, photoanodes can also be prepared using coating techniques. Drop-coating is conducted by dropping the precursor on the substrate (Fig. 4d), while spin-coating is operated using a spin-coater and can achieve a more uniform film (Fig. 4e). Electrospinning is a promising technique to synthesize nanofiber structure non-TiO_2-based photoanodes. In the presence of a high voltage electric field, the liquid supply device promotes the flow of the electrospinning precursor, and a large amount of solvent volatilizes to produce spray, forming micro-nanofibers on the substrates (Fig. 4f).

Coating methods are popular in the *ex situ* preparation of photoanodes. For instance, Fan and coworkers[44] prepared MoS_2 nanosheets *via* liquid exfoliation, dispersed them in ethanol *via* sonication, and then drop-cast them onto TiO_2 electrodes. Notably, g-C_3N_4-based photoanodes are often prepared using *ex situ* methods because g-C_3N_4 is usually prepared by heating melamine or urea. For instance, Sun *et al.*[37] first obtained MgO/g-C_3N_4 powder by calcining mixed alkaline magnesium carbonate and melamine in a muffle furnace, which was subsequently mixed with ethanol and Nafion and then loaded onto FTO by the coating method. Perylene diimide (PDI), a promising organic semiconductor, was also loaded onto indium–tin-oxide (ITO) glass by the dip-coating method.[45] Therefore, *ex situ* methods allow sought-after materials to be coated onto the substrates and to exert their strengths, significantly expanding the variety of non-TiO_2-based photoanodes.

Exploiting the relatively mild operating conditions and low equipment costs (refer to Table 1 and Fig. 3b), wet-chemical methods predominate in the current synthesis of non-TiO_2-based photoanodes (see Fig. 3a). Electrodes produced *via* this methodology are extensively utilized for the degradation of

Table 1 Comparison of different *in situ* synthesis methods of non-TiO_2-based photoanodes

Category	Synthesis method	Photoanode	Modification method	Synthesis condition[a]	Main equipment	Pollutant (mg L^{-1})	Removal efficiency	Stability of photoanode	Ref.
Wet-chemical methods	Hydrothermal	hm-m-WO_3/W mesh	Heterophase junction	160 °C for 12 h	Teflon-lined stainless-steel autoclave; oven	BPA[b] (20)	99.9% (150 min) 60.9% (TOC, 150 min) k = 0.054 min^{-1}	Still removed 99.8% of BPA, 5 cycles	46
		NiFe-LDH[c]/**Co_3O_4**/Ni foam	Heterojunction	90 °C for 8 h		BPA (10) Cr(VI) (10)	100% (120 min) ~65 (TOC, 120 min)	Still removed more than 90% BPA and Cr(VI), 10 cycles	47
		α-Fe_2O_3/g-C_3N_4/FTO[d]	Heterojunction	120 °C for 4 h at pH 1.0		CA[e] (30)	99.7% (300 min)	Still removed 98% of CA, 5 cycles	48
	Chemical bath deposition	WO_{3-x}/FTO	Doping	85 °C for 2 h	Beaker; constant temperature heating magnetic stirrer	4-CP[f] (10)	98.9% (180 min) k = 0.016 min^{-1}	Insignificant decrease in activity, 8 cycles	49
		MoO_3/**ZnO**/Zn	Heterojunction	90 °C for 4 h		Phenol (40) Cu^{2+} (200)	89.5% (COD, 240 min) 93.5% (Cu^{2+}, 240 min)	Insignificant decrease in activity, 4 cycles	50
		WO_3/Ag/FTO	Modifying with noble metals	90 °C for 3 h		Hg^{2+} (40.12)	100% (12 min)	Kept photocurrent stable at pH 2, 200 min	51
	Liquid phase deposition	Cu_2O/**α-Fe_2O_3**/FTO	Heterojunction	55 °C for 30 min	Beaker; constant temperature heating magnetic stirrer	OTC[g] (10)	73.3% (60 min) k = 0.021 min^{-1}	About 3% loss of PEC activity, 5 cycles	42
		α-Fe_2O_3/Ti Ni-**ZnO**/FTO	Doping	40 °C for 1.5 h		TC[h] (10)	87.5% (180 min)	Not mentioned	52
	Successive ionic layer adsorption and reaction	$BiVO_4$/**α-Fe_2O_3**/FTO	Morphological modification and heterojunction	Room temperature, normal pressure	Beaker	Phenol (50)	68.89% (COD, 120 min)	Photocurrent density decayed by ~8%, 7000 s	53
		ZnS/Bi_2S_3/ZnONR array/FTO	Heterojunction	Room temperature, normal pressure		H_2 production	112.8 μmol cm^{-2} h^{-1}	~70% retention of initial photocurrent density, 2 h	54
		Ag_2S/$BiVO_4$/FTO	Heterojunction	Room temperature, normal pressure		CIP[i] (10)	80% (120 min) 69% (TOC, 120 min)	Insignificant decrease in activity, 3 cycles	55
	Drop-coating	Sn/Ti:α-Fe_2O_3@**Cu_xO**/FTO	Doping and heterojunction	60 °C for 5 min	Beaker; constant temperature heating magnetic stirrer	MO[j]	99% (120 min)	Kept photocurrent steady, 10 h	56
		BiClO/Ti	No modification	Room temperature for 1 h		RhB[k] (10)	89% (180 min)	Kept photocurrent steady, 3 h	57
	Spin-coating	**$BiVO_4$**/FTO	No modification	2000 rpm for 15 s, 15 cycles		UO_2^{2+} (20); TC (20)	100% (UO_2^{2+}, 40 min) 99% (TC, 40 min)	Insignificant decrease in activity, 20 cycles	58
	Electrospinning	$BiFeO_3$/**$BiVO_4$**/Al	Heterojunction	12 kV, 0.01 mL min^{-1}	Electrostatic spinning machine	RhB (10)	90.88% (180 min)	Insignificant decrease in activity, 15 h	59
		Pd-**ZnO**/CNF/FTO	Modifying with noble metals	15 kV, 0.5 mL min^{-1}, 300 rpm		Paracetamol (15.12)	100% (150 min) k = 0.009 min^{-1} 71.2% (TOC, 240 min)	Less than 4% loss of PEC activity, 8 cycles	60
Electro-chemical methods	Anodic oxidation	Fe_2WO_6/**ZnO**/Zn	Heterojunction	1.1 V for 2 h	DC[l] power supply	TC (20), total nitrogen (5.1)	100% (TC, 120 min) 88.4% (total nitrogen, 120 min)	~20% loss of PEC activity, 5 cycles	61
		CN-**WO_3**/W	Modifying with carbonaceous materials	70 V	DC power supply	PFOA[m] (5)	95% (120 min)	Kept current stable, 24 h	62
		WO_3 nanostructures	Morphological modification	20 V, 50 °C for 4 h, hydrodynamic condition (375 rpm)	Rotating disk electrode	ATZ[n] (20)	100% (180 min) k = 0.023 min^{-1}	Not mentioned	63
	Electro-chemical deposition	O_v-Fe_2O_3@**$BiVO_4$**/FTO	Heterojunction	−0.1 V (*vs.* Ag/AgCl), 5 min	Electrochemical workstation	COD (320), NH_3–N (59.2)	89.38% (COD, 2 h) 100% (NH_3–N, 2 h)	Still removed 84.75% of COD, 4 cycles	64
		Ar-**Fe_2O_3**/Ti^{3+}-TiO_2-NTs	Heterojunction	Switch between the cathode pulse (0.25 A,	Electrochemical workstation	TC (20)	100% (90 min) k = 0.0684 min^{-1}	Still removed 99.5% of TC, 5 cycles	65

Table 1 (*continued*)

Category	Synthesis method	Photoanode	Modification method	Synthesis condition[a]	Main equipment	Pollutant (mg L^{-1})	Removal efficiency	Stability of photoanode	Ref.
				10 ms) and the anode pulse (0.25 A, 3 ms)					
		O_v:$BiVO_4$/FTO	Oxygen vacancy	No details	DC power supply	Triethanolamine (0.5 M)	The faradaic efficiency of H_2 production is 97.26%	Kept current stable, 6 h	31
Other chemical methods	Atomic layer deposition	**Pd**-ZnO/CNF/FTO	Modifying with noble metals	Pre-heated at 220 °C	Low-pressure thermal ALD[o] reactor	Paracetamol (15.12)	100% (150 min) k = 0.009 min^{-1} 71.2% (TOC, 240 min)	Less than 4% loss of PEC activity, 8 cycles	60
		Sn-Fe_2O_3/**NiFeO$_x$**/FTO	Doping	106.66 Pa, 125 °C–225 °C, N_2 atmosphere	In-house built flow-type ALD reactor	TC (20)	96% (120 min) k = 0.024 min^{-1}	Kept photocurrent steady, 18 cycles	66
	Chemical vapor deposition	NTAs/**g-C_3N_4**	Morphological modification and heterojunction	550 °C for 4 h (5 °C min^{-1})	Ceramic crucible	Aniline (10)	31% (60 min)	Almost no decreases in PEC performances, 5 cycles	67
		N-**ZnO**/Si	Doping	700 °C for 45 min	CVD reactor	MB[p] (5)	95% (90 min)	~10% loss of PEC activity, 5 cycles	68
Physical methods	Sputtering	$BiVO_4$/FTO	Doping	2.0 Pa, O_2/Ar flow rate: 40/100 sccm, 300/250 W	Sputter gun	TC (20)	79% (12 min)	Kept photocurrent steady, ~8000 s	69

[a] Some photoanodes involve the combination of multiple catalysts and require more than one preparation method. The catalyst synthesis condition mentioned is only for a certain catalyst. When involving multiple catalysts, the words representing the target catalyst are thickened. In addition, the conditions here do not include post-processing conditions. [b] BPA: bisphenol A. [c] NiFe-LDH: NiFe-layered double hydroxide. [d] FTO: fluorine-doped tin oxide. [e] CA: clofibric acid. [f] 4-CP: 4-chlorophenol. [g] OTC: oxytetracycline. [h] TC: tetracycline hydrochloride. [i] CIP: ciprofloxacin. [j] MO: methyl orange. [k] RhB: rhodamine B. [l] DC: direct current. [m] PFOA: perfluorooctanoic acid. [n] ATZ: atrazine. [o] ALD: atomic layer deposition. [p] MB: methylene blue.

organic compounds, the reduction of heavy metals, and the generation of energy. Nevertheless, Fig. 3a indicates that the convenience of wet-chemical methods is often accompanied by low stability, particularly in the cases of SILAR and LPD, with an average electrode lifetime of less than 500 min. This lack of stability may be attributed to inadequate adhesion and the occurrence of oxygen evolution reaction (OER) alongside the oxidation of contaminants.[70] In contrast, the photoanodes synthesized through hydrothermal methods and electrospinning techniques demonstrate relatively high stability. He *et al.*[71] employed a combination of metal-assisted chemical etching and hydrothermal methods to fabricate a Si/ZnO photoanode for application in PFCs. The resulting system maintained the ability to degrade over 90% of RhB after 20 cycles (7200 min), showcasing remarkable stability.

4.2 Electrochemical methods

Electrochemical methods are less reliant on specialized equipment and harsh conditions, allowing for precise adjustments in film thickness by varying electrolysis conditions. Anodic oxidation operates by applying a positive voltage to clean metal foils, sheets, or rods, followed by annealing to obtain the corresponding metal oxide semiconductor (Fig. 4g). For instance, Fernández-Domene and coworkers[63] prepared a WO_3 photoanode with nanostructures by adding H_2O_2 to the electrolyte. The charge transfer resistance of this nanostructure was significantly lower than that of the WO_3 compact layer, which was prepared without H_2O_2. Similarly, ZnO and Fe_2O_3 photoanodes can also be synthesized using this method. This approach reduces interfacial resistance between the film and the substrate[72] by enabling the direct formation of nanostructures while ensuring good stability. Feng *et al.*[73] demonstrated that the current of their photoanode remained stable for 40 days.

In contrast to anodic oxidation, the electrochemical deposition method applies a negative voltage, facilitating the deposition of anions from the electrolyte onto conductive substrates (Fig. 4h). In the preparation of the $BiVO_4$ photoanode, Zheng *et al.*[74] initially deposited BiOI onto the FTO substrate. Subsequently, they coated the precursor with a solution of $VO(acac)_2$ in dimethyl sulfoxide (DMSO) solution and immersed it in NaOH solution following the annealing process. This methodology allows for the deposition on various substrates, not limited to the corresponding metal, as FTO and other conductive electrodes can also be utilized. Furthermore, the deposition process is not confined to metal oxide semiconductors.

As shown in Fig. 3a, electrochemical deposition has a very wide application in the preparation of non-TiO_2-based photoanodes (second only to the hydrothermal method), and the electrodes prepared by electrochemical methods are moderately stable. Moreover, electrochemical methods can be carried out using electrochemical workstations or even DC power supplies, and the cost is not high (see Fig. 3b).

4.3 Other chemical methods and physical methods

In addition to the above chemical methods, several photoanode preparation techniques are not commonly used in wastewater treatment. ALD is a method of forming thin films by alternating

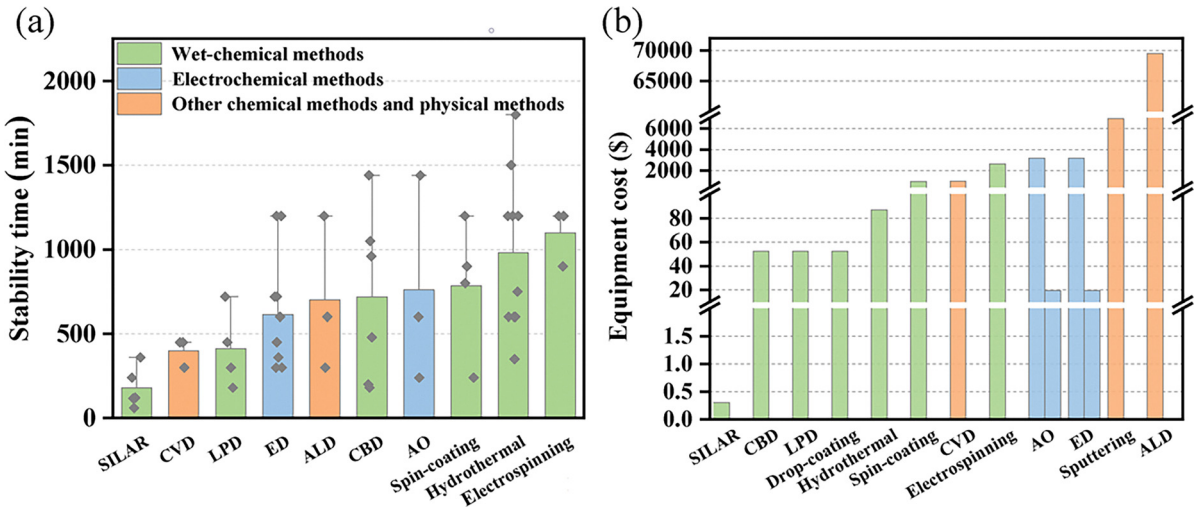

Fig. 3 (a) The stability duration of the photoanodes prepared by different methods was provided from the literature. Based on the cycling experiments or photocurrent–time curves mentioned in the literature, the total number of minutes of stability tests carried out is considered to be the stable duration of the photoanode if there is no significant decrease in activity during the test period (drop-coating and sputtering methods are not shown because there are fewer than three references). (b) The cost of equipment required to prepare non-TiO_2-based photoanodes. AO (anodic oxidation) and ED (electrochemical deposition) can be operated using an electrochemical workstation and a DC power supply, so there are two prices for them. The price of the equipment is from **https://www.16888.com**, and the lowest price of the same type of product is selected for comparison.

pulses of gas-phase precursors into a reaction chamber and gas–solid-phase chemisorption reactions on the surface of the substrate (Fig. 4i). The films prepared by this method have excellent 3D conformality, stability, and homogeneity. Through ALD, Kim's group[66] formed a $NiFeO_x$ film on the surface of Fe_2O_3 to achieve surface reconstruction. At the same time, they attained an accurate stoichiometric ratio using the super-cycle method. The as-prepared photoanode was used for water splitting and degradation of TC; as a result, it showed great PEC performance and could maintain a stable photocurrent after 18 cycles. However, as shown in Table 1 and Fig. 3b, this preparation method requires a special ALD reactor, which limits its application due to its high cost.

CVD is a technology employed for the precise fabrication of photoanodes. This method utilizes substances in gaseous or vaporous states, which react at a gas–solid interface to yield solid deposits (Fig. 4j). Compared with wet-chemical methods, films produced *via* CVD exhibit superior adherence to the substrate, and the control over film thickness is highly manageable. Mane *et al.*[68] reported the development of an N–ZnO–Si photoanode fabricated through metal–organic chemical vapor deposition (MOCVD) employing a nitrogen-doping technique. This approach effectively addressed the challenges of wide bandgap and low resistance to photo-corrosion of ZnO nanowires. As illustrated in Fig. 3a, however, the high cost associated with this method does not yield a corresponding enhancement in electrode stability.

Sputtering is an uncommon physical method that involves bombarding the source material (metal or metal oxide) under vacuum conditions with energetic ions and depositing atoms onto the substrate[75] (Fig. 4k). Benefiting from its large-scale coating ability, non-selectivity of the substrate, high controllability, and versatility, sputtering has been widely applied in the industry; hence, it is a promising technique for preparing photoanodes used for wastewater treatment in the future. For instance, Huang *et al.*[69] prepared a $BiVO_4$ photoanode with excellent performance by co-sputtering V and $BiVO_4$ targets, demonstrating excellent removal ability for TC (79% within 12 min). In addition, to demonstrate scalability, they prepared a large-area $BiVO_4$ (100 × 100 mm), offering additional insights for promoting the proposed photoanode toward the practical application of PEC degradation. However, the expensive and specialized equipment (Fig. 3b) and harsh operating conditions prevent it from being extensively studied at the laboratory scale.

4.4 Modification of photoanodes

Pristine photoanodes may suffer from problems including large bandgap energy, low stability, or easy recombination of photo-induced carriers, so it is necessary to modify photoanodes. Typical modification methods for non-TiO_2-based photoanodes include morphological modification, doping modification, heterojunction construction, and modification with carbonaceous materials, noble metals, and other co-catalysts. Modification can be achieved during the preparation of photoanodes, and the corresponding preparation methods are listed in Table 1 and Fig. 5.

The morphological modification encompasses geometric shape control, nanometer-scale adjustments, and facet engineering, as illustrated in Fig. 4l. Variations in catalyst dimensionality result in distinct properties. For instance, Co_3O_4 predominantly exhibits a one-dimensional (1D) nanowire structure,[76] whereas and MoS_2 is characterized as a typical two-dimensional (2D) material.[77] 1D fibers or tubes possess a reduced charge carrier diffusion distance, which effectively inhibits the recombination of e^- and h^+; conversely, 2D sheets demonstrate high adhesion, facilitating reactions with organic contaminants.[78] The crystal structure of a semiconductor significantly influences its

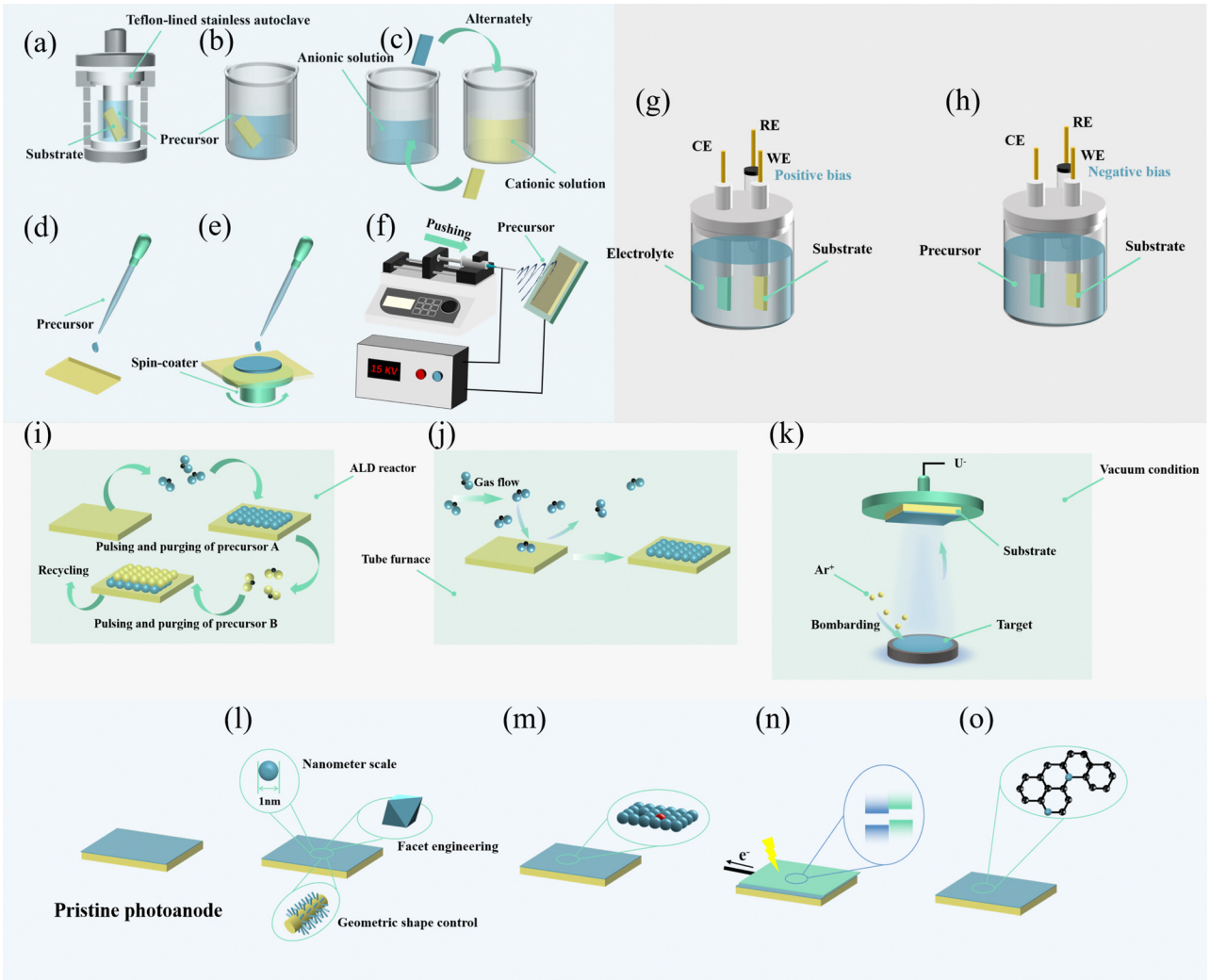

Fig. 4 Synthesis and modification methods for non-TiO_2-based photoanodes. Wet-chemical methods: (a) hydrothermal method; (b) CBD and LPD; (c) SILAR; (d) drop-coating; (e) spin-coating; and (f) electrospinning. Electrochemical methods: (g) anodic oxidation and (h) electrochemical deposition. Other chemical methods: (i) ALD and (j) CVD. Physical methods: (k) sputtering. Modification methods: (l) morphological modification; (m) doping modification; (n) heterojunction; and (o) combining with co-catalysts.

properties, including stability, adsorption capacity, and photocatalytic reactivity.[79–81] $BiVO_4$ has garnered considerable attention in the realm of crystal facet engineering. For example, Yang *et al.*[81] fabricated SnO_2/010 facet-exposed $BiVO_4$ nanocomposites utilizing the hydrothermal method. Their findings indicated that (010) facet-exposed $BiVO_4$, in comparison to the (100) facets, exhibits higher surface energy and more exposed Bi atoms. Consequently, augmenting the exposure ratio of the (010) facet is advantageous for enhancing the adsorption of 2,4-dinitrophenol.

The doping modification includes metal doping and non-metal doping, and sometimes the construction of defects is also considered (Fig. 4m). Wu *et al.*[82] devised a photoanode with simultaneous boron doping and oxygen vacancie (OV) production on the $Bi_2Sn_2O_7$ photoanode. The synergistic effects of B-doping and OVs narrowed the bandgap of $Bi_2Sn_2O_7$, allowed the surface of $Bi_2Sn_2O_7$ to be more electron-rich and created intermediate levels inhibiting the recombination of e^-–h^+ pairs. As a result, it exhibited efficient and stable PEC degradation of SMT.

Constructing heterojunctions is one of the most popular strategies to modify photoanodes (Fig. 5) because it can effectively separate e^-–h^+ pairs by a built-in electric field (Fig. 4n). In addition to heterojunctions, some scholars have studied other forms of interface composites; for instance, Huang and Zhang's group[83] synthesized a $BiVO_4$ homojunction with staggered band alignment without incorporating any heteroatoms. Furthermore, Wang and coworkers[84] fabricated a black/red phosphorus *in situ* junction, which was further utilized to prepare a novel multi-heterojunction TiO_2–$BiVO_4$–BP/RP film.

Combining photoanodes with co-catalysts is also a perspective strategy (Fig. 4o), for example, Wang *et al.*[51] demonstrated that the deposition of Ag on WO_3 facilitated the simultaneous reduction and detection of Hg within a concentration range of 0.296 nM to 12.5 μM when the electrode was operated in a

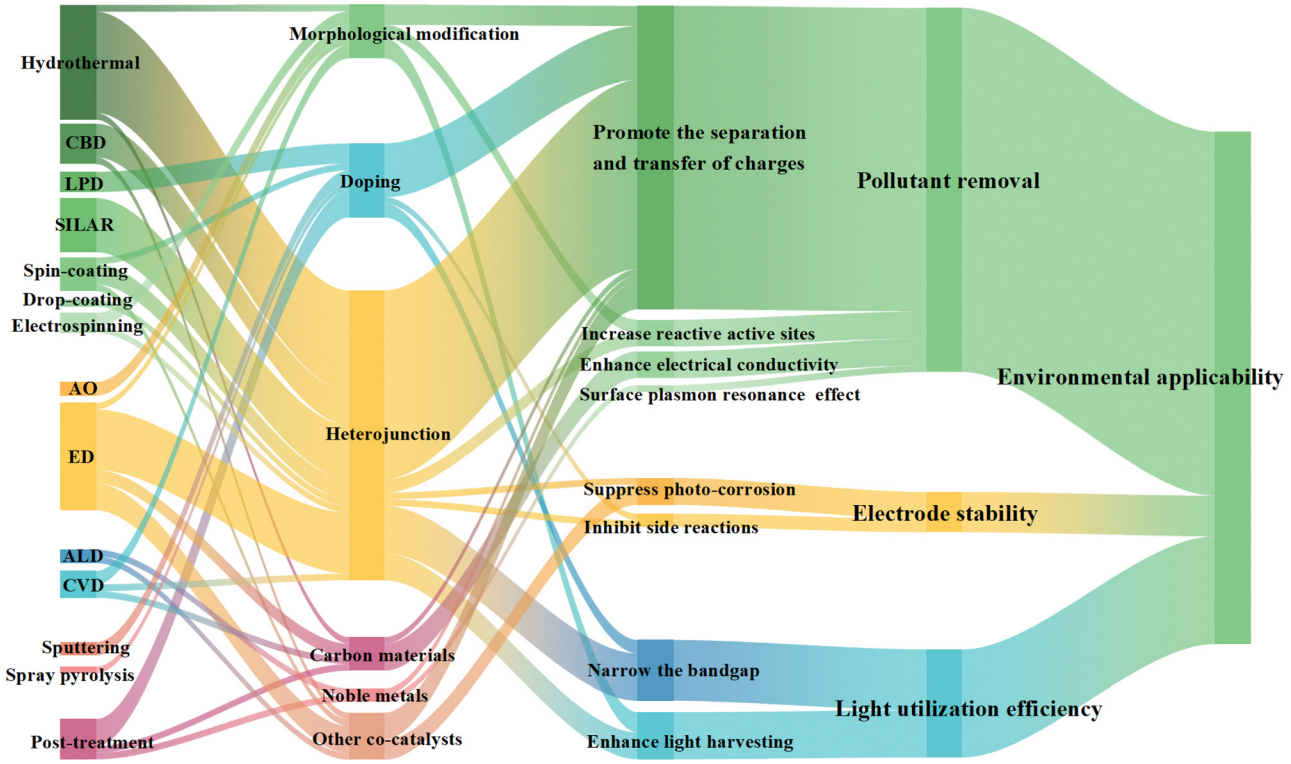

Fig. 5 The synthesis–structure–mechanism–activity relationship diagram of non-TiO_2-based photoanodes based on literature statistics. (The results of the Sankey diagram are derived from 76 pieces of literature on non-TiO_2-based photoanodes for pollutant wastewater treatment.)

solution containing Hg^{2+}. This approach achieved a remarkable removal efficiency of 97 ± 2% for Hg^{2+} in industrial wastewater containing various pollutant ions. Furthermore, PEC performance can be significantly enhanced through the incorporation of carbonaceous materials, attributed to their superior electrical conductivity.[85] Additionally, the introduction of co-catalysts has been shown to accelerate sluggish kinetics and electron transfer processes.[86,87]

Notably, certain modification approaches, though less commonly employed in PEC wastewater treatment systems, deserve attention for their potential to enhance photoanode performance. A prominent example is surface reconstruction. Seenivasan *et al.*[66] demonstrated this strategy by applying an ultra-thin $NiFeO_x$ catalyst coating to hematite photoanodes *via* ALD. Benefiting from ALD's precise thickness control, the conformal $NiFeO_x$ coating not only passivated surface states but also facilitated rapid charge transfer to the electrolyte. This strategy effectively suppressed e^-–h^+ recombination within the photoanode.

5. Performance evaluation of non-TiO_2-based photoanodes

Different preparation methods yield photoanodes with distinct structures, which in turn influence the electrode's performance in various ways. The evaluation of photoanode performance includes pollutant removal efficiency, electrode stability, light utilization efficiency, and environmental applicability. In order to further investigate how different structures affect electrode performance, the underlying mechanisms were characterized. A synthesis–structure–mechanism–activity diagram for non-TiO_2-based photoanodes was developed after an extensive literature review (Fig. 5).

5.1 Pollutant removal efficiency

Contaminant degradation experiments are the most commonly used method to test photoelectrodes. The pollutant removal efficiencies of prepared electrodes under different operational parameters are compared. Although higher light source power generally favors contaminant removal, our group has opted for lower-power LED lights from an energy consumption perspective, achieving satisfactory results.[14,37,88] Anodic bias is another critical parameter. While higher bias voltages enhance the separation of photogenerated carriers by external electric fields and increase dark current density, excessively high bias may compromise anode stability and raise energy consumption.[5] No clear patterns emerge regarding non-TiO_2-based photoanode performance across varying pH levels. For instance, the WO_3/TiO_2 photoanode prepared by Li *et al.*[19] exhibited optimal urea degradation at pH 3, whereas the Fe_2WO_6/ZnO photoanode prepared by Lam *et al.*[61] achieved peak TC degradation at pH 7, with such variations attributable to differences in both pollutant and photoanode properties. Additionally, this discrepancy may also be influenced by the dominant active species. For example, in the TC treatment system reported by Sun *et al.*,[37] where $^1O_2$ acts as the primary reactive species, the photoanode

exhibits continuously enhanced performance within the pH range of 7–9.

These degradation experiments under varied conditions determine the optimal operational parameters for photoanodes. To demonstrate the superiority of the developed photoanodes, researchers further conduct comparative evaluations with other electrodes. However, variations in experimental conditions and lack of standardized testing methods make it difficult to compare and evaluate the published results. In order to assess the practical application potential of electrodes rationally, the attention must be paid to the selection of water matrix. Most photoanodes perform well in solutions containing deionized water, simple-component electrolytes, and target contaminants, while actual water has a complex composition that can reduce the efficiency. For instance, Rather *et al.*[89] collected sewage from three different treatment locations in Hong Kong to use as the electrolyte in PEC experiments. The results showed that sewage with extremely high concentrations of Cl^- and SO_4^{2-} reduced charge (h^+) transport, thereby decreasing degradation efficiency. It is also reasonable to consider how co-existing ions affect degradation efficiency or to simulate pollutants in real wastewater as comprehensively as possible. Wu *et al.*[90] investigated the effect of co-existing anions on the degradation of SMT in their PEC system and found that the order of effect of the co-existing anions was $PO_4^{3-} > CO_3^{2-} > Cl^-$ (Fig. S1, ESI†). Zhang *et al.*[91] constructed a 4-liter reactor and used ammonia, glucose, bovine serum albumin, and *E. coli* to represent inorganic matter, organic matter, macromolecules, and microbial pollutants contained in wastewater, respectively. The results showed that large protein molecules were much more difficult to destroy than *E. coli*. Alternatively, from another perspective, researchers can use some bulky indicators when expressing degradation efficiency, such as total organic carbon (TOC), chemical oxygen demand (COD), and biochemical oxygen demand (BOD), which are common in actual wastewater treatment. Therefore, the selection of actual wastewater as a contaminant, the consideration of the influence of co-existing ions, or the selection of bulky indicators can help to evaluate the performance of photoanodes more comprehensively.

5.2 Stability of photoanodes

Another fundamental purpose of studying photoanodes for actual wastewater treatment is to assess their stability after repeated use. The most common methods for characterizing the stability of photoanodes are illustrated in Fig. S2 (ESI†).

In PEC wastewater treatment, studies identifying the causes of stability loss are limited. The Fourier-transform infrared (FTIR) spectra of the MoS_2@BL-$BiVO_4$ photoanode, after recycling tests in sewage, displayed new peaks compared with those observed after use in a NaCl solution. These peaks were attributed to the adsorption of natural organic matter (NOM) as noted by Zheng *et al.*[92] The review of Zuo *et al.*[93] clarified that the stability of electrodes is influenced by an electrochemical window and organic fouling or inorganic scaling. Understanding the key factors influencing the stability of photoanodes can help formulate strategies to maintain their performance. Liu *et al.*[94] identified that the primary cause of photoanode deactivation is the reconstruction of the oxide surface structure, which occurs due to the coordination of the oxide with Cl^- during seawater splitting. They further enhanced the stability of the β-Fe_2O_3 photoanode by improving the metal–oxygen interaction. By introducing Sn into the crystal lattice, the Sn/β-Fe_2O_3 photoanode demonstrated stability during seawater splitting for 3000 h. Li *et al.*[95] modified the $BiVO_4/Cu_2O$ heterojunction photoanode by using the co-catalyst cobalt–phosphate (Co–Pi). Co–Pi can effectively capture and release holes through the chemical state change of Co, which, in turn, inhibits photo-corrosion and improves electrode stability (Fig. S2h, ESI†). In summary, the stability of the photoanode can be improved by inhibiting the occurrence of both side reactions and photo-corrosion (Fig. 5).

Moreover, the cycling tests are mainly performed in the laboratory and use solutions containing certain target contaminants. Tests in real applications or using sewage are insufficient, and stability results may change under such conditions.

5.3 Light utilization efficiency

The enhancement of light harvesting through specialized geometrical structures and the reduction of the bandgap width of photocatalysts can significantly improve the sunlight utilization of photoanodes (Fig. 5). The most common indicators used to evaluate light utilization efficiency, along with corresponding examples, are summarized in eqn (S1)–(S4) and Fig. S3 (ESI†). Among these indicators, internal quantum efficiency (IQE) reflects the intrinsic efficiency of the material, while η accounts for the contribution of the external bias voltage. Altogether these two indicators effectively represent the light utilization efficiency of non-TiO_2-based photoanodes. Furthermore, the evaluation methods primarily stem from PEC water splitting, and there is currently no established evaluation system for PEC wastewater treatment. Here, we refer to the commonly used equations (eqn (S3) and (S4) (ESI†)) for PEC water splitting and propose the photoelectrochemical mineralization efficiency (PME) by considering both pollutant degradation efficiency and externally input electrical energy, as shown in eqn (1):

$$\mathrm{PME} = \left[\frac{\dfrac{-\Delta G^0 \cdot \Delta\mathrm{TOC} \cdot V}{12 \times 1000nCAt} - P_\mathrm{E}}{P_\mathrm{L}}\right] \times 100\% \qquad (1)$$

Herein, ΔG^0 is the standard Gibbs free energy change (J mol^{-1}) for the complete mineralization of pollutants, ΔTOC is the concentration of TOC removed (mg L^{-1}), V is the volume of the reaction solution (L), nC is the number of carbon atoms in the pollutant, A is the effective reaction area of the electrode (m^2), t is the reaction time (s), P_E is the power consumed by the external bias (W m^{-2}), and P_L is the incident radiation power (W m^{-2}).

5.4 Environmental applicability

The aforementioned metrics ultimately serve the environmental applicability of photoanodes, *i.e.*, their application potential. Life cycle assessment (LCA) systematically evaluates

the environmental impact of products throughout their life cycle by quantifying resource consumption, energy use, and environmental emissions. For example, Gao *et al.*[96] prepared a $NbClO_x/BiVO_4$ photoanode using an electrochemical deposition method, which directly synthesized ClO^- from seawater while simultaneously recovering high-value-added products. In the LCA of this work, the functional unit was defined as 1 kg of NaClO, and indicators such as fossil abiotic depletion potential, human toxicity potential, and global warming potential were used to quantify the environmental impact. Compared with dimensionally stabilized anodes, the $NbClO_x/BiVO_4$ photoanode reduced CO_2 emissions by 75.31% and lowered electricity costs by 77.16% when producing the same amount of ClO^- using conventional grid electricity. Zhang *et al.*[97] developed a system that utilized electrons generated from PEC phenol degradation for cathodic ammonia synthesis. LCA results indicated that electricity consumption was the only critical factor affecting its overall economic and sustainability performance. Compared with standalone electrochemical ammonia synthesis, the integrated system reduced electricity consumption by 51.8% and exhibited lower greenhouse gas emissions.

In studies on non-TiO_2-based photoanodes, LCA applications remain limited, with most research focusing only on greenhouse gas emissions during pollutant degradation or techno-economic analyses. In the work conducted by Zheng *et al.*[74] on reduced $BiVO_4$ photoanodes for simultaneous organic pollutant degradation, ammonia nitrogen removal, bacterial inactivation, and hydrogen production, they categorized PEC process carbon emissions into direct and indirect emissions. Indirect emissions were linked to PEC electricity consumption and were compensated using the energy of the produced H_2; the compensated electricity consumption was multiplied by the emission factor to calculate the indirect emissions. Techno-economic analyses typically calculate electricity consumption per unit volume of wastewater treated,[14,98] per unit mass of pollutant removed[46,99] or per order of pollutant concentration reduction.[5] Notably, these analyses often focus solely on pollutant degradation, while electrode preparation also requires significant energy input, such as kilowatt-level oven usage for hydrothermal reactions, far exceeding the energy demands of electrochemical deposition. When the entire life cycle is considered, evaluation outcomes may differ. Additionally, most experiments are not conducted under direct sunlight, and simulated light sources consume significantly more energy than the electricity required to drive PEC processes,[5] which is often overlooked during techno-economic analyses and deserves attention as well.

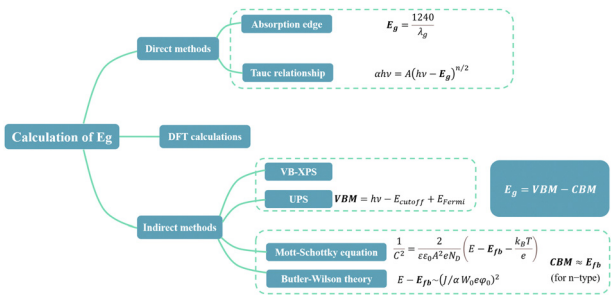

Fig. 6 Methods for the determination of E_g.

6. Mechanism characterization of PECs

To reveal how modified catalysts improve PEC performance, the study of the PEC mechanism is needed; thus, the characterization methods to reveal the mechanism are deep-level and vital work.

6.1 Light absorption and exciton excitation

The crux of this process is to determine the light absorption efficiency of the semiconductor (see Section 5.3) and its bandgap energy (E_g).

E_g calculation methods can be divided into three categories: direct methods, indirect methods, and DFT calculations (Fig. 6). An introduction to these methods, along with corresponding examples, is summarized in eqn (S5)–(S12) and Fig. S4 (ESI†).

Table 2 presents the bandgap energy of some non-TiO_2-based photoanodes. It is evident that the E_g values differ from

Table 2 The bandgap energy and carrier's lifetime and corresponding characterization methods of some non-TiO_2-based photoanodes

Photoanode	Calculation method	E_g (eV)	Carrier lifetime	Calculation method	Ref.
hm-m-WO_3/W mesh	Tauc plot	2.87	6.21 ns	TRPL	46
$WO_3/BiVO_4$/FTO	Not mentioned	Not mentioned	22.7 ms (transit time)	IMPS	105
$BiVO_4$/ITO	Tauc plot	2.45	Not mentioned	Not mentioned	12
	DFT	2.23			
$BiVO_4$/FTO	Tauc plot; M–S plot, UPS	2.54	Not mentioned	Not mentioned	106
SnO_2@$BiVO_4$/FTO	Tauc plot; M–S plot, UPS	2.46	Not mentioned	Not mentioned	86
$Ir_xZn_{1-x}O$/Ti	Tauc plot; DFT	1.42–2.26	0.5 ms (charge relaxation time)	EIS	107
MgO/g-C_3N_4/FTO	Tauc plot	3.34	5.67 ns	TRPL	37
α-Fe_2O_3/g-C_3N_4/FTO	Tauc plot	2.08	4.2 ms	EIS	48
Sn-Fe_2O_3/NFO25/FTO	Tauc plot	2.20	Not mentioned	Not mentioned	66
ZnO/CdS/MoS_2/FTO	Tauc plot	2.25	10 ns	TPV	108
MoS_2/Ti	Not mentioned	1.80	Not mentioned	Not mentioned	77
In_2O_3/In_2S_3/CdS/FTO	Tauc plot	~1.80	3.12 ns	TRPL	41
$BiVO_4/Cu_2O$/Co–P/FTO	Tauc plot	~2.40	Not mentioned	OCP	95
Cu_2O/Ag_3PO_4/FTO	Tauc plot	Not mentioned	47.8 ms	EIS	109
$BiVO_4$@TiO_2/Ti	Tauc plot	2.98	17.45 ns	TRPL	110

the pristine E_g shown in Fig. 2a, which is attributed to the modification of catalysts. Additionally, the Tauc plot is the most widely used method for calculating E_g, yet few studies employ more than one method to calculate E_g. Since the E_g, CBM, and VBM positions are crucial for explaining the reaction mechanism, researchers must characterize this information in a mutually verifiable manner. Moreover, it is important to consider the suitability of characterization methods prior to conducting analysis. For instance, UV-vis DRS is not appropriate for semiconductors with intermediate energy states, which are often caused by defects.[23] Additionally, the Kubelka–Munk function may introduce uncertainty in the analysis of doped semiconductors.[100,101]

6.2 Separation and transfer of carriers

6.2.1 Separation efficiency. Charge separation efficiency can be indicated by carrier density, which is derived from the slope of the Mott–Schottky (M–S) plot using eqn (2) (taking an n-type semiconductor as an example):[102]

$$N_D = \frac{2}{e\varepsilon\varepsilon_0} \times \frac{dE}{d\frac{1}{C^2}} \quad (2)$$

The meaning of each symbol has been explained in eqn (S10) and (S11) (ESI†). Some researchers used N_D to approximate carriers' density,[48] and it is inversely related to the slope of the Mott–Schottky plot (Fig. 7a).

The photocurrent is an important indicator to imply carrier density and separation efficiency. Chronoamperometry is usually used to reveal how photocurrent changes over time; current (density)–time curves (Fig. S6a, ESI†) and transient photocurrent (density) (Fig. S6b, ESI†) are two main forms of it. LSV (Fig. S6c, ESI†) and chopped LSV (Fig. S6d, ESI†) are usually used to depict how photocurrent changes with applied potential. The measurement of photocurrent in different electrolytes can be used to calculate charge separation efficiency according to eqn (3):[103]

$$\eta_{sep} = \frac{j_{PEC}}{j_{abs}\eta_{inj}} \quad (3)$$

where η_{sep} is the charge separation efficiency, j_{PEC} is the measured photocurrent, j_{abs} is the maximum possible photocurrent density, and η_{inj} is the charge separation efficiency. When the photoanode is tested in Na_2SO_3 solution (a kind of hole scavenger; some studies use H_2O_2 to scavenge holes[104]), sulfite oxidation kinetics is fast, and η_{inj} can be estimated to be 100%, then η_{sep} can be written as eqn (4):

$$\eta_{sep} = \frac{j_{Na_2SO_3}}{j_{abs}} \quad (4)$$

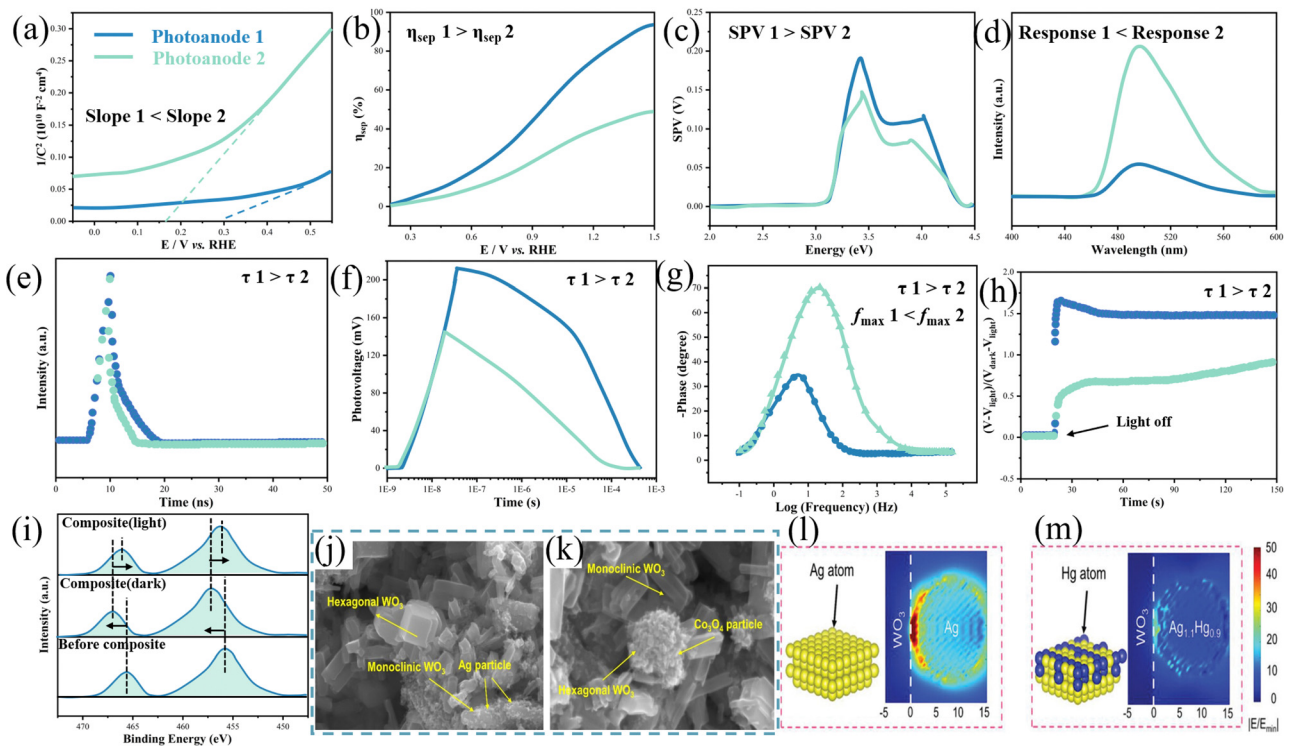

Fig. 7 Techniques used to characterize separation efficiency: schematic diagram of (a) the Mott–Schottky plot, (b) charge separation efficiency, (c) steady-state SPV results, and (d) steady-state PL spectra (where it is assumed that the separation efficiency of photoanode 1 is higher than that of photoanode 2); charge transfer kinetics: schematic diagram of (e) TRPL decay spectra, (f) transient photovoltage result, (g) Bode plot, and (h) normalized OCP decay curves (where it is assumed that photoanode 1 has a longer decay lifetime than photoanode 2); charge transfer pathway: (i) schematic XPS spectra of the composite photoanode under different conditions, (j) and (k) SEM images of the WO_3 photoanode after photochemical deposition of Ag and Co_3O_4, reprinted from ref. 46, Copyright (2022), with permission from Elsevier. (l) and (m) DDA simulations for the electric field intensity at the WO_3 nanoplate and Ag nanocrystal interface before and after Hg^{2+} pretreatment, reprinted with permission from ref. 51 Copyright (2023) Wiley-VCH.

and j_{abs} can be calculated using eqn (5) and (6):

$$j_{abs} = \int_0^{\lambda_0} J_{flux}(\lambda)\mathrm{d}\lambda \quad (5)$$

$$J_{flux}(\lambda) = \frac{eN_{ph}(\lambda)}{h\nu(\lambda)}\mathrm{LHE}(\lambda) \quad (6)$$

Herein, λ_0 is the absorption edge of the photoanode, J_{flux} is the current flux, N_{ph} is the photon flux and can be obtained from the spectrum of the light; and $h\nu$ is the energy of the photon. After obtaining the above information, the η_{sep} plot of the photoanode at different bias potentials can be plotted (Fig. 7b). For example, Wang *et al.*[103] found that the charge separation efficiency of GaN:ZnO photoanodes increases with decreasing moisture exposure time; corresponding information is shown in Fig. S7 (ESI†).

In addition to the photocurrent, as shown in Scheme 1, the e^-–h^+ pairs generated by the light excitation of the photoanode create a surface photovoltage (SPV) after separation within the SCL. The steady-state SPV reflects the separation efficiency of the photogenerated charges at the surface/interface (Fig. 7c).[111] PL spectra can also be used to analyze separation efficiency, as the recombination of h^+ and e^- results in photon emission; a smaller PL response indicates more efficient charge separation (Fig. 7d). Finally, DFT can provide insights into the separation and migration properties of charges by calculating the effective masses of holes and electrons since the efficiency of charge separation and migration is inversely proportional to the effective mass.[112]

6.2.2 Charge transfer kinetics. The carrier lifetime is defined as the time required for the e^-–h^+ pairs to decay to 1/e through radiative recombination.[113] Time-resolved photoluminescence spectroscopy (TRPL) is a technique for probing the dynamics of time-dependent changes in the excited state radiative excitation spectra of a semiconductor under pulsed monochromatic light irradiation. A slower decay represents a longer lifetime (Fig. 7e). Jin *et al.*[110] prepared a $BiVO_4$ quantum dot-decorated TiO_2 photoanode, and TRPL was employed to investigate the separation and transfer dynamics of e^-–h^+ pairs. The results showed that the modified photoanode exhibited a longer decay lifetime, suggesting that more e^-–h^+ pairs can participate in the surface reaction. The transient surface photovoltage (TPV) test, a system based on SPV using a pulsed laser as the light source, can also be used to determine carrier lifetimes (Fig. 7f).[108] Moreover, Bode plots of EIS can assist in calculating carrier lifetimes (Fig. 7g). Arotiba's group investigated electron lifetime according to eqn (7):[109]

$$\tau = \frac{1}{2\pi f_{max}} \quad (7)$$

where f_{max} is the peak frequency of the Bode plot. Open circuit potential (OCP) decay curves can be used to determine the potential-dependent carrier lifetime of photoanodes.[95] In the test, the photoanode is initially illuminated by a light source to generate charge carriers. After turning off the light source, the voltage decay is measured over time (Fig. 7h). The carriers' lifetime can be calculated using eqn (8):

$$\tau = \left(\frac{k_B T}{e}\right)\left(\frac{\mathrm{d}_{OCP}}{\mathrm{d}t}\right)^{-1} \quad (8)$$

Lastly, similar to the form of eqn (7), Zeng *et al.*[114] carried out intensity-modulated photocurrent spectroscopy (IMPS) to measure the majority charge carrier transit time—the average time required for the photogenerated carriers to reach the back contact of the substrate—of their WO_3/$BiVO_4$ photoanode, as described in eqn (9):

$$\tau_d = \frac{1}{2\pi f_{min}} \quad (9)$$

where f_{min} is the frequency at the minimum value in the IMPS plot.

However, characterizing the lifetime of photoinduced carriers is complex due to various factors. First, do different techniques yield similar results for the same catalysts? As shown in Table 2, the carrier lifetimes calculated using TRPL and TPV are in the nanosecond range, while those obtained from EIS and IMPS are in the millisecond range. It is crucial to determine whether this significant discrepancy arises from the catalysts themselves or the characterization methods employed. Additionally, the literature presents conflicting explanations regarding the relationship between carrier lifetime and separation efficiency. Gao *et al.*[10] argued that the shorter lifetime measured *via* TRPL indicated more effective photoexcited charge separation and transfer. Similarly, Song *et al.*[15] suggested that the shorter lifetimes of photogenerated holes measured through transient absorption spectra (TAS) also reflects an efficient charge separation and transfer process. These interpretations contradict the aforementioned view that longer lifetimes signify more effective separation. When considering the time carriers spent in the external circuit or at the interface of the photoanode and solution, a shorter carrier lifetime suggests faster transfer and more efficient utilization. However, when examining transfer within the bulk of the photoanode, a longer lifetime implies reduced recombination. Therefore, it is essential to compare measurement techniques for carrier lifetimes to enhance the credibility of results, and the interpretation of these results should be as clear as possible.

6.2.3 Charge transfer pathway. The charge transfer pathway varies depending on the structure of the catalysts. Heterojunctions and other composite structures can protect vulnerable photocatalysts, enhance light harvesting efficiency, and improve the separation of photogenerated carriers. Once the composite structure is formed, it is crucial to understand the charge transfer at the interface of the different catalysts. XPS can be employed to characterize the heterojunction formation and the direction of electron transfer during the PEC process (Fig. 7i). An increase in the binding energy of the tested element after composite formation indicates that this material loses electrons during the formation of the composite structure. In *in situ* XPS, electron transfer in the tested material also occurs upon light application to the photoanode. For example, a decrease in the

binding energy after photoexcitation suggests that electrons in the composite are transferred from another material to this tested material under illumination. Wu *et al.*[90] utilized *in situ* and *ex situ* XPS spectra to elucidate the formation of the $Bi_2Sn_2O_7$ quantum dot/TiO_2 S-scheme heterojunction.

Apart from these methods, Li and coworkers[46] synthesized photoanodes featuring WO_3/W heterophase junction structures, significantly enhancing the separation of photoinduced h^+ and e^-. They proposed a matched band structure for monoclinic WO_3 and hexagonal WO_3 based on the results of UV-vis DRS and Mott–Schottky curves, further verifying their assumption through photochemical deposition experiments. As shown in the SEM images in Fig. 7j and k, the deposition of Ag nanoparticles on monoclinic WO_3 and the formation of Co_3O_4 nanoparticles on hexagonal WO_3 indicated the accumulation of e^- and h^+, respectively, which aligned with the charge transfer pathway they proposed.

WO_3/Ag Schottky heterojunction photoanodes were prepared by Wang *et al.*[51] Under light exposure, hot electrons were generated at the interface of WO_3 and Ag due to the localized surface plasmon resonance (LSPR) effect. However, this effect was quenched upon the combination of Ag and Hg^{2+}. As a result, the corresponding photocurrent decreased, enabling both the reduction of Hg and the simultaneous detection of Hg concentration. Utilizing discrete dipole approximation (DDA) simulations, they explored the spatial distribution of the LSPR-induced electric field. In the absence of Hg^{2+}, the WO_3–Ag interface exhibited the highest electric field enhancement (EFE) (Fig. 7l). Conversely, in the presence of Hg^{2+}, the formation of surface $Ag_{2-x}Hg_x$ resulted in diminished oscillation and polarization, leading to reduction in EFE (Fig. 7m).

Furthermore, internal electric fields (IEF) are commonly referenced in discussions of charge separation in PECs; hence, characterizing IEF is crucial for understanding the intrinsic mechanisms involved. Recently, Yuan's group[115] concluded characterization techniques to identify IEF. These techniques include determining the work function of semiconductors using UPS, Kelvin probe force microscopy (KPFM), and DFT calculations, as well as measuring the surface potential through KPFM, piezo-response force microscopy (PFM), and SPV. Additionally, they indirectly demonstrated the formation of IEF through free radical quenching experiments and electron paramagnetic resonance (EPR) studies.

6.3 Interface reaction process

This process is influenced by two factors. The first factor is the electrode itself, which includes its redox capacity, the active species produced, and the interfacial charge transfer rate. The second factor is the contaminant, encompassing its mass transfer processes, adsorption characteristics, and reactive sites.

When the applied bias is low and is used solely to accelerate the separation of e^-–h^+ pairs, the redox ability is primarily determined by the band position of the photocatalyst. The positions of the VB and CB can be determined using various methods described in Section 5.2.1. Under certain conditions, once the bandgap of semiconductors is determined, it can also facilitate the calculation of the conduction band minimum (CBM) and valence band maximum (VBM). For instance, Yang *et al.*[116] calculated the VB potential of C_3N_4–MoS_2 using eqn (10):

$$\mathrm{VBM} = X - E_e + 0.5E_g \quad (10)$$

where X is the absolute electronegativity of the semiconductor and E_e is the energy of free electrons on the hydrogen scale. Similarly, Shao and coworkers[117] determined the band edge positions of CBM and VBM using eqn (11) and (12):

$$\mathrm{CBM} = -\Phi + 0.5E_g \quad (11)$$

$$\mathrm{VBM} = -\Phi - 0.5E_g \quad (12)$$

By comparing the band edge position with the potentials of various redox reactions, we can deduce possible reactions and reactive species. As the applied potential increases, it is important to consider electro-oxidation or electro-reduction.[118]

Like other AOPs, in PECs, some reactions are dominated by reactive species, while others may be influenced more by electron transfer following surface adsorption. The primary reactive species utilized in non-TiO_2-based PECs include radicals such as hydroxyl radicals ($^{\bullet}OH$) and superoxide radicals ($O_2^{\bullet-}$). Occasionally, chlorine radicals ($Cl^{\bullet}$),[40] chlorite radicals ($ClO^{\bullet}$),[119] sulfate radicals ($SO_4^{\bullet-}$),[44] carbonate radicals ($CO_3^{\bullet-}$),[120] and others are considered when PECs are combined with other AOPs. The nonradical pathway typically involves the participation of h^+, e^-, and sometimes singlet oxygen ($^1O_2$).[121] To assess the contributions of these reactive species, researchers commonly employ quenching experiments, probe techniques, and EPR to characterize the roles of these species qualitatively and quantitatively. However, some researchers have proposed that adding high-concentration ROS quenchers may alter the catalytic mechanisms within their systems.[122] Moreover, in the PEC process, quenching of holes or electrons can enhance contaminant removal efficiency by promoting the separation of holes and electrons.[81] Recently, Yang's group[123] supplemented the reaction rate constants of probes and quenchers with commonly used reactive species, and general recommendations were put forward for the selection of appropriate probes and quenchers.

Several techniques can be employed to characterize interfacial charge transfer efficiency. As noted in eqn (3) and (4), charge injection efficiency can be derived from eqn (13):

$$\eta_{inj} = \frac{j_{PEC}}{j_{Na_2SO_3}} \quad (13)$$

η_{inj} indicates the efficiency of hole injection into the electrolyte, with higher charge injection efficiency reflecting better utilization of accumulated h^+. Furthermore, the photocurrent response curve can help diagnose surface oxidation kinetics. For example, Shao's group[86] designed a SnO_2@$BiVO_4$ photoanode, but its photocurrent response curve exhibited a noticeable spike, indicating that h^+ accumulated on the surface of the photoanode. To address this issue, they introduced a Co–Pi cocatalyst, significantly improving the charge injection efficiency (Fig. 8a). Tafel curves can characterize interfacial charge kinetics by plotting the relationship between current density and overpotential on a

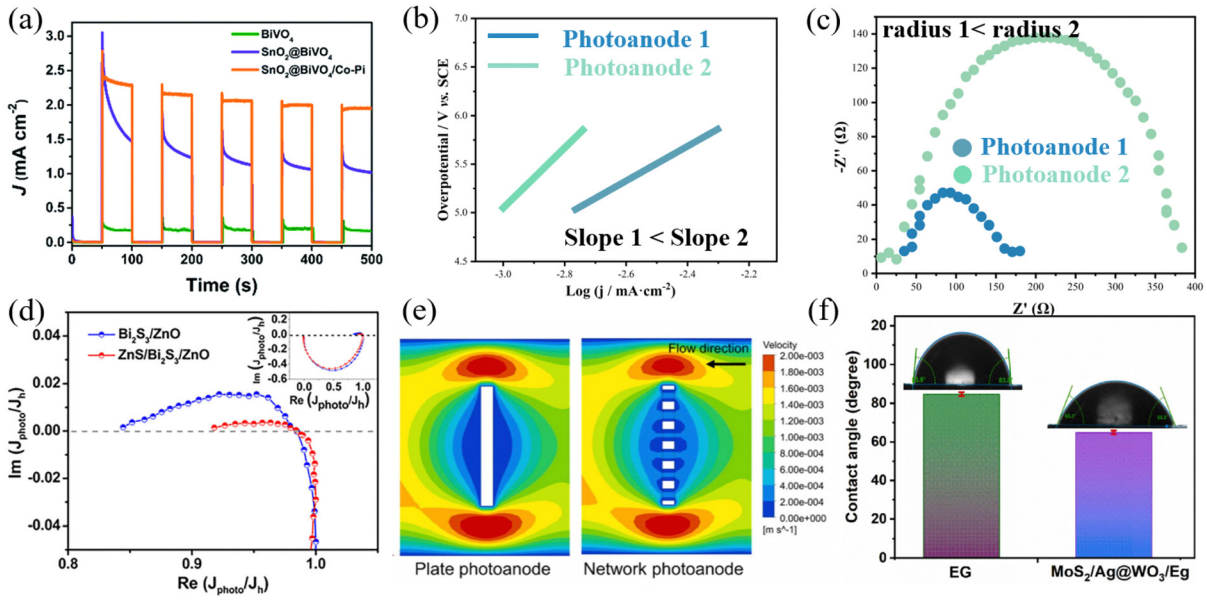

Fig. 8 Techniques for characterizing interfacial reaction processes: (a) photocurrent–time curves of pristine $BiVO_4$, SnO_2@$BiVO_4$, and SnO_2@$BiVO_4$/Co–Pi photoanodes, reprinted with permission from ref. 86, Copyright (2019) Royal Society of Chemistry. Schematic diagram of (b) Tafel curves and (c) Nyquist plots (where it is assumed that photoanode 1 has faster interfacial charge transfer kinetics than photoanode 2). (d) IMPS Nyquist plots of the Bi_2S_3/ZnO NRA and ZnS/Bi_2S_3/ZnO NRA, respectively, reprinted with permission from ref. 54, Copyright (2022) American Chemical Society. (e) CFD simulations of the flow velocity in the plate and network electrode in flowing water, reprinted from ref. 46, Copyright (2022), with permission from Elsevier. (f) Contact angle of EG and MoS_2/Ag@WO_3/EG photoanodes, reprinted from ref. 124, Copyright (2023), with permission from Elsevier.

semi-logarithmic scale. A lower Tafel slope indicates faster charge transfer kinetics and reduced polarization resistance (Fig. 8b).[76] The arc at low frequency in Nyquist plots is attributed to charge transfer at the electrode–electrolyte interface (Fig. 8c), with a smaller arc signifying faster surface reaction kinetics.[117] Moreover, Lu *et al.*[54] carried out IMPS to assess h^+ injection efficiency into the electrolyte. In the corresponding IMPS Nyquist plots (Fig. 8d), the low-frequency intercept in the first quadrant for the ZnS/Bi_2S_3/ZnO photoanode is larger than that of the Bi_2S_3/ZnO photoanode, resulting in greater h^+ injection efficacy and photocurrent density.

Mass transfer at the interface of the pollutant electrode can be calculated using computer simulations. To analyze the fluid behavior around the electrode, Ma *et al.*[46] conducted computational fluid dynamics (CFD) simulations on both the plate electrode and the WO_3/W mesh electrode. As shown in Fig. 8e, the grids in the mesh electrode enhanced fluid flow and facilitated contact between the contaminant and the catalyst compared to the plate electrode.

To investigate the adsorption of pollutants at the electrode, N_2 adsorption–desorption isotherms can help to determine the specific surface area.[46,81] FTIR provides insights into the adsorption mechanism,[81] and contact angle measurements can evaluate hydrophobicity. Mafa *et al.*[124] synthesized a visible light-responsive MoS_2/Ag@WO_3/EG photoanode. They compared bare EG and MoS_2/Ag@WO_3/EG photoanodes using contact angle measurements; the results showed that the contact angles of the two were 84.76° and 64.87°, respectively (Fig. 8f). A smaller contact angle indicates better hydrophilicity, facilitating full contact between the anode and pollutant molecules and enhancing the generation of •OH from water molecules on the electrode surface.

The electronic structure of pollutants can help to understand the degradation mechanisms. The highest occupied molecular orbital (HOMO), lowest unoccupied molecular orbital (LUMO), and Fukui index are commonly used to describe the charge distribution of organic contaminants.[125] For instance, Zhang *et al.*[48] employed DFT simulation to illustrate the HOMO and LUMO orbital distributions, charge distribution, and Fukui index of clofibric acid. Their simulated results facilitated predictions regarding the feasibility of specific sites in clofibric acid for free radical attacks. By integrating their computational findings with data from a high-resolution mass spectrometer, they proposed pathways for the catalytic degradation of clofibric acid.

7. Conclusion and perspectives

7.1 Conclusion

In recent years, non-TiO_2-based photoanodes used for wastewater treatment have been a field of interest for researchers and have undergone rapid development. Given that the reasonable synthesis of photoanodes can help achieve the best performance of photocatalysts, comprehensive evaluation can help to reasonably analyze the application prospects, and sufficient characterization can help to intuitively understand the intrinsic mechanisms; this review introduces the synthesis, evaluation, and characterization methods of non-TiO_2-based photoanodes used for wastewater treatment.

Compared with TiO_2-based photoanodes, different non-TiO_2-based photoanodes have potential applications in various

scenarios. For example, WO_3, g-C_3N_4, $BiVO_4$, and Fe_2O_3 have the potential for visible light response; WO_3, ZnO, and Fe_2O_3 have numerous applications in PFC; and WO_3, $BiVO_4$, and their composites are suitable for the removal of ammonia nitrogen.

The techniques for electrode synthesis include wet-chemical methods, electrochemical methods, other chemical methods, and physical methods. When considering practical applications, it is important to evaluate the cost of the synthesis method, the stability of the electrode, and the potential for large-scale production. Currently, the wet-chemical and electrochemical methods are the most commonly used methods for synthesizing non-TiO_2-based photoanodes. However, overly simple operating conditions may compromise electrode stability. In contrast, the less commonly used physical method is costly but offers large-scale coating capabilities.

When evaluating the effect of electrode degradation on pollutants, it is necessary to pay attention to the ability of the photoanode to treat actual sewage. When assessing stability, it is also essential to identify the key factors affecting it. When evaluating light utilization efficiency, it is necessary to develop more sophisticated equations to incorporate pollutant degradation and electrical energy input. Finally, the assessment of the environmental applicability of the photoanode is indispensable, as it determines the potential for its practical application.

To deeply reveal the mechanism of PEC wastewater treatment, the bandgap of the catalyst should be confirmed through various methods. Additionally, the separation efficiency, carrier kinetics, and transfer pathways of the carriers should be further investigated. It is also important to consider the redox ability of the electrode interface, as well as the physical and chemical conversion processes of pollutants during PEC wastewater treatment.

Despite the aforementioned recommendations for photoanode synthesis and a systematic summary of non-TiO_2-based photoanode evaluation and characterization methods, several fundamental questions still remain in the following areas.

7.2 Perspectives: from the atomic level to large-scale applications

The synthesis, evaluation, and characterization of non-TiO_2-based photoanodes should be closely interconnected. The synthesis method influences the evaluation and characterization results, while the characterization outcomes can, in turn, enhance the synthesis approach. This review paper proposes a comprehensive overview of synthesis, evaluation, and characterization methods, spanning from the micro-level to the electrode level and extending to large-scale applications (Scheme 2).

(i) At the micro-level, synthesizing catalysts should prioritize the micro-morphology of photocatalysts, the regulation of exposed crystal facets, and the enhancement of synergy among different components in composite materials. It is also important to improve the dispersion and utilization efficiency of cocatalysts, such as single-atom catalysts (SACs). Furthermore, there are some catalysts with excellent performance in PEC water splitting that can be considered for PEC wastewater treatment. For instance, Ta_3N_5 exhibits potential in photocatalytic pollutant removal due to its superior visible-light responsiveness (E_g = 2.1 eV)[126] and low raw material supply risk.[127] Notably, its lower valence band position[128] makes it more suitable for constructing heterojunctions with other photocatalysts.[129,130]

To better understand the catalyst structure at the atomic level, more advanced characterization methods should be introduced, for example, electron microscopy with higher resolution (*e.g.*, high-angle angular dark field-scanning transmission electron microscopy (HAADF-STEM)), electron microscopy that changes the properties of the photoanode as little as possible during observation (*e.g.*, cryogenic electron microscopy (cryo-EM)), and energy spectroscopy that can analyze finer coordination environments (*e.g.*, extended X-ray absorption fine structure (EXAFS)). Furthermore, to infer the mechanism of photoanode action more intuitively, it is necessary to represent the changes in the photoanode during the PEC water treatment process; therefore, *in situ* characterization techniques are very

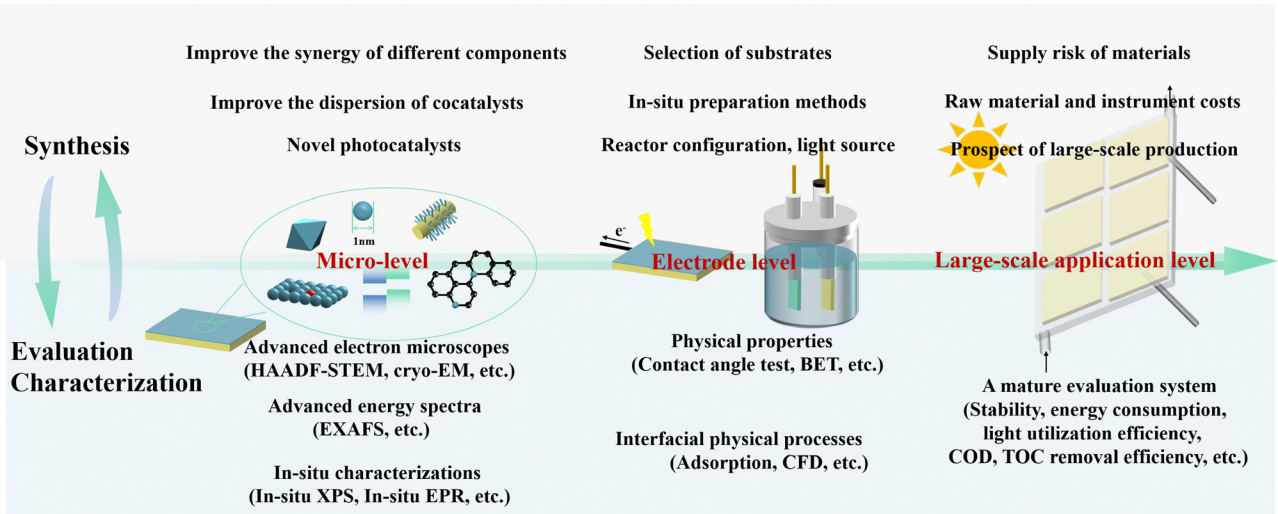

Scheme 2 Perspective of the synthesis, evaluation and characterization of photoanodes.

important. *In situ* photoelectrochemical characterization should be performed while the PEC system degrades pollutants, and *in situ* characterization results can also be obtained by controlling the input light and voltage.

(ii) At the electrode level, maximizing catalyst efficiency requires careful consideration of the most suitable substrate, including factors such as conductivity and stability of the catalyst film. The *in situ* growth method should be chosen for preparing the photoanode. Additionally, the selection of reactor configuration, electrolyte, and light source will also impact the efficiency of non-TiO_2-based photoanodes.

Correspondingly, attention should also be given to characterizing the physical properties of the photoanode, including hydrophobicity, specific surface area, and interface resistance, as well as the interfacial physical processes related to pollutants, such as adsorption and mass transfer.

(iii) At the large-scale application level, although researchers have made attempts to carry out degradation under sunlight and prepare large-area electrodes (see Sections 3 and 4.3), there are currently few large-scale applications for PEC wastewater treatment. From the perspective of electrode preparation, the challenges that limit scale-up mainly include equipment that does not support large-area preparation, time-consuming preparation methods, and the high costs of catalysts and substrates. To address these difficulties, researchers could employ scalable preparation methods such as sputtering, modularly produce small-area electrodes for assembly into large-area electrodes,[131] and select metal foils, sheets, or rods rather than conductive glass as electrode substrates. What's more, it is also worth considering the supply risk of PEC materials, with Hillenbrand *et al.*[127] showing that hematite is the material with the lowest current supply risk, while bismuth vanadate has the highest future supply risk.

At this level, attention to characterization and evaluation should not focus solely on pollutant removal efficiency. A photoanode with strong stability, low energy consumption, or high light utilization efficiency can also enhance its overall performance. Additionally, the degradation of a single target pollutant may produce more toxic byproducts, making high degradation efficiency appear misleadingly one-sided. Thus, it is essential to develop a more comprehensive evaluation system that encompasses multiple dimensions.

(iv) Notably, machine learning is instructive in both the synthesis and characterization of photoanodes, enhancing the interaction and feedback between synthesis and characterization methods. For instance, screening suitable photocatalysts or substrates quickly and accurately is a massive task, while machine learning can help solve this problem. It can not only guide the screening, preparation, and optimization of new catalysts under different environmental application scenarios by combining the data obtained from different routes but also improve the analysis of characterization results by integrating characterization techniques, such as electron microscope image recognition and extraction of information from wave spectra.

Once the aforementioned suggestions are addressed, it will greatly benefit the development of photoelectrocatalysis in the environmental field. This will advance the preparation of photoanodes for industrial applications and enhance deeper mechanistic characterization. We anticipate that this review will inspire more frontier research in the synthesis, evaluation, and characterization of non-TiO_2-based photoanodes, thereby attracting significant attention in the field of PEC wastewater treatment.

Conflicts of interest

There are no conflicts of interest to declare.

Data availability

No primary research results, software or code have been included and no new data have been generated or analyzed in this review.

Acknowledgements

This work was supported by the National Key Research and Development Program International Cooperation Project (2023YFE0108100), Tianjin Research Innovation Project for Postgraduate Students (2022SKY005), and Fundamental Research Funds for the Central Universities, Nankai University.

References

1 W. Xiong, H. Guo, Y. Liu, Y. Meng, Y. Jiang, B. Li, R. Liu and C. Yang, *Chem. Eng. J.*, 2024, **489**, 151389.
2 G. Ren, M. Zhou, Q. Zhang, X. Xu, Y. Li and P. Su, *Chem. Eng. J.*, 2020, **387**, 124037.
3 Y. Xie, Q. Rong, F. Mao, S. Wang, Y. Wu, X. Liu, M. Hao, Z. Chen, H. Yang, G. I. N. Waterhouse, S. Ma and X. Wang, *Nat. Commun.*, 2024, **15**, 2671.
4 F. Li, K. Liu, Y. Bao, Y. Li, Z. Zhao, P. Wang and S. Zhan, *Water Res.*, 2024, **254**, 121373.
5 J. Liu, R. Liang, Z. Hu, X. Zhang and M. Zhou, *Chem. Eng. J.*, 2024, **491**, 152088.
6 B. Li, H. Pan and B. Chen, *Water Res.*, 2023, **244**, 120537.
7 S. Li, J. Xie, J. Gu and M. Zhou, *Chin. Chem. Lett.*, 2023, **34**, 108204.
8 F. Deng, H. Olvera-Vargas, M. Zhou, S. Qiu, I. Sirés and E. Brillas, *Chem. Rev.*, 2023, **123**, 4635–4662.
9 S. Li, W. Wang, H. Wu, X. Zhang, R. Liang, X. Zhang, G. Song, J. Jing, S. Li and M. Zhou, *Proc. Natl. Acad. Sci. U. S. A.*, 2024, **121**, e1890002175.
10 C. Gao, J. Low, R. Long, T. Kong, J. Zhu and Y. Xiong, *Chem. Rev.*, 2020, **120**, 12175–12216.
11 Q. Zhou, Y. Guo and Y. Zhu, *Nat. Catal.*, 2023, **6**, 574–584.
12 F. Li, W. Zhao and D. Y. C. Leung, *Appl. Catal., B*, 2019, **258**, 117954.
13 V. Andrei, G. M. Ucoski, C. Pornrungroj, C. Uswachoke, Q. Wang, D. S. Achilleos, H. Kasap, K. P. Sokol, R. A. Jagt, H. Lu, T. Lawson, A. Wagner, S. D. Pike, D. S. Wright,

R. L. Z. Hoye, J. L. MacManus-Driscoll, H. J. Joyce, R. H. Friend and E. Reisner, *Nature*, 2022, **608**, 518–522.
14 R. Liang, H. Wu, Z. Hu, J. Sun, C. Fu, S. Li, X. Zhang and M. Zhou, *Appl. Catal. B-Environ. Energy*, 2024, **352**, 124042.
15 R. Song, H. Chi, Q. Ma, D. Li, X. Wang, W. Gao, H. Wang, X. Wang, Z. Li and C. Li, *J. Am. Chem. Soc.*, 2021, **143**, 13664–13674.
16 Y. Zhang, Y. Ji, J. Li, J. Bai, S. Chen, L. Li, J. Wang, T. Zhou, P. Jiang, X. Guan and B. Zhou, *J. Hazard. Mater.*, 2021, **402**, 123725.
17 Y. Yu and H. Huang, *Chem. Eng. J.*, 2023, **453**, 139755.
18 R. Dhawle, D. Mantzavinos and P. Lianos, *Appl. Catal., B*, 2021, **299**, 120706.
19 L. Li, J. Li, F. Fang, Y. Zhang, T. Zhou, C. Zhou, J. Bai and B. Zhou, *Appl. Catal., B*, 2023, **333**, 122776.
20 M. B. Costa, M. A. de Araújo, M. V. D. L. Tinoco, J. F. D. Brito and L. H. Mascaro, *J. Energy Chem.*, 2022, **73**, 88–113.
21 S. Garcia-Segura and E. Brillas, *J. Photochem. Photobiol., C*, 2017, **31**, 1–35.
22 L. Y. Ozer, C. Garlisi, H. Oladipo, M. Pagliaro, S. A. Sharief, A. Yusuf, S. Almheiri and G. Palmisano, *J. Photochem. Photobiol., C*, 2017, **33**, 132–164.
23 F. Parrino, V. Loddo, V. Augugliaro, G. Camera-Roda, G. Palmisano, L. Palmisano and S. Yurdakal, *Catal. Rev.: Sci. Eng.*, 2019, **61**, 163–213.
24 X. Wang, H. Xu, Y. Nan, X. Sun, J. Duan, Y. Huang and B. Hou, *J. Oceanol. Limnol.*, 2020, **38**, 1018–1044.
25 Z. Zhang and J. T. Yates, *Chem. Rev.*, 2012, **112**, 5520–5551.
26 R. Das Adhikari, M. J. Patel, H. Baishya, D. Yadav, M. Kalita, M. Alam and P. K. Iyer, *Chem. Soc. Rev.*, 2025, **54**, 3962–4034.
27 S. Corby, R. R. Rao, L. Steier and J. R. Durrant, *Nat. Rev. Mater.*, 2021, **6**, 1136–1155.
28 J. Zhu, D. Shao, W. Wen, Z. Tian, X. Zhang and S. Wang, *Coord. Chem. Rev.*, 2024, **518**, 216095.
29 M. Li, Y. Liu, L. Dong, C. Shen, F. Li, M. Huang, C. Ma, B. Yang, X. An and W. Sand, *Sci. Total Environ.*, 2019, **668**, 966–978.
30 Z. Hu, M. Zhou, H. A. Maitlo, R. Liang, Y. Zheng, H. Wu, X. Song and O. A. Arotiba, *Appl. Catal., B*, 2023, **331**, 122676.
31 Z. Wang, X. Liu, Y. Mao, H. Zhang, P. Wang, Z. Zheng, Y. Liu, Y. Dai, H. Cheng, Z. Wang and B. Huang, *Adv. Funct. Mater.*, 2024, **34**, 2313950.
32 C. Dong, Y. Yang, X. Hu, Y. Cho, G. Jang, Y. Ao, L. Wang, J. Shen, J. H. Park and K. Zhang, *Nat. Commun.*, 2022, **13**, 4982.
33 T. Tong, M. Zhang, W. Chen, X. Huo, F. Xu, H. Yan, C. Lai, W. Wang, S. Hu, L. Qin and D. Huang, *Coord. Chem. Rev.*, 2024, **500**, 215498.
34 P. Jiang, T. Zhou, J. Bai, Y. Zhang, J. Li, C. Zhou and B. Zhou, *Water Res.*, 2023, **235**, 119914.
35 H. Ullah, Z. Haneef, A. Ahmad, I. S. Butler, R. Nasir Dara and Z. Rehman, *Inorg. Chem. Commun.*, 2023, **153**, 110775.
36 X. Pang, R. Liu, X. Lv, W. Lu, L. Sun, Q. Wang, Z. Li, Q. Kang, J. Xie, Y. Pang and F. Zhou, *RSC Adv.*, 2024, **14**, 32883–32892.
37 J. Sun, H. Wu, C. Fu, C. Zhang, Z. Hu and M. Zhou, *Appl. Catal. B-Environ. Energy*, 2024, **351**, 123976.
38 C. Xie, Q. Zhang, Q. Zeng, Q. Zhang, Y. Liu, G. Tang, J. Lv, T. Yu and Q. Zeng, *Chem. Eng. J.*, 2024, **480**, 148363.
39 Z. Yan, W. Kuang, Y. Lei, W. Zheng, H. Fu, H. Li, Z. Lei, X. Yang, S. Zhu and C. Feng, *Environ. Sci. Technol.*, 2023, **57**, 20915–20928.
40 Y. Zhang, J. Cui and Y. Pei, *Chem. Eng. J.*, 2023, **464**, 142652.
41 Y. Xiao, G. Tian, Y. Chen, X. Zhang, H. Fu and H. Fu, *Appl. Catal., B*, 2018, **225**, 477–486.
42 L. Cheng, Y. Tian and J. Zhang, *J. Colloid Interface Sci.*, 2018, **526**, 470–479.
43 S. P. Ratnayake, J. Ren, J. van Embden, C. F. McConville and E. Della Gaspera, *J. Mater. Chem. A*, 2021, **9**, 25641–25650.
44 X. Fan, Y. Zhou, G. Zhang, T. Liu and W. Dong, *Appl. Catal., B*, 2019, **244**, 396–406.
45 H. Miao, J. Yang, G. Peng, H. Li and Y. Zhu, *Sci. Bull.*, 2019, **64**, 896–903.
46 Q. Ma, R. Song, F. Ren, H. Wang, W. Gao, Z. Li and C. Li, *Appl. Catal., B*, 2022, **309**, 121292.
47 W. Fei, J. Gao, N. Li, D. Chen, Q. Xu, H. Li, J. He and J. Lu, *J. Hazard. Mater.*, 2021, **402**, 123515.
48 L. Zhang, X. Zhang, C. Wei, F. Wang, H. Wang and Z. Bian, *Chem. Eng. J.*, 2022, **435**, 134873.
49 X. Liu, H. Zhou, S. Pei, S. Xie and S. You, *Chem. Eng. J.*, 2020, **381**, 122740.
50 S. Lam, J. Sin, H. Zeng, H. Lin, H. Li, Z. Qin, J. W. Lim and A. R. Mohamed, *Sep. Purif. Technol.*, 2021, **265**, 118495.
51 J. Wang, S. Liu, T. Liu, J. Wang, F. Liu, M. Jia, J. Li, Y. Lai, Y. Zhao, L. Jiang, Y. Li and T. Zhai, *Adv. Funct. Mater.*, 2023, **33**, 2302809.
52 J. Feng, Y. Tian, O. K. Okoth, L. Cheng and J. Zhang, *J. Electrochem. Soc.*, 2019, **166**, H685–H690.
53 L. Xia, J. Bai, J. Li, Q. Zeng, L. Li and B. Zhou, *Appl. Catal., B*, 2017, **204**, 127–133.
54 Y. Lu, R. Popescu, D. Gerthsen, Y. Feng, W. Su, Y. Hsu and Y. Chen, *ACS Appl. Mater. Interfaces*, 2022, **14**, 7756–7767.
55 B. O. Orimolade and O. A. Arotiba, *Sci. Rep.*, 2020, **10**, 5348.
56 L. R. Nagappagari, J. Lee, H. Lee, B. Jeong and K. Lee, *Environ. Pollut.*, 2021, **271**, 116318.
57 K. Li, Y. Xu, Y. He, C. Yang, Y. Wang and J. Jia, *Environ. Sci. Technol.*, 2013, **47**, 3490–3497.
58 Q. Zhang, Q. Deng, Y. Zhang, Y. Xiao, C. Zhang, H. Gong, Q. Zeng, Q. Zhang and Q. Zeng, *Appl. Catal. B-Environ. Energy*, 2024, **347**, 123808.
59 P. Teng, J. Zhu, X. Wen, Z. Li, S. Gao, K. Li, N. Copner, Z. Liu, H. Jiang, Y. Zhang and F. Tian, *Opt. Mater.*, 2023, **146**, 114318.
60 A. A. Nada, B. O. Orimolade, H. H. El-Maghrabi, B. A. Koiki, M. Rivallin, M. F. Bekheet, R. Viter, D. Damberga, G. Lesage, I. Iatsunskyi, E. Coy, M. Cretin, O. A. Arotiba and M. Bechelany, *Appl. Mater. Today*, 2021, **24**, 101129.
61 S. Lam, J. Sin, H. Zeng, H. Li, H. Lin, L. Huang, J. Lim and K. Dong, *Sep. Purif. Technol.*, 2024, **329**, 125249.

62 D. Zhang, W. Zhang, J. Zhang, L. Dong, X. Chen, Y. Guan, Z. Wang and Y. Li, *Chem. Eng. J.*, 2024, **480**, 147910.
63 R. M. Fernández-Domene, R. Sánchez-Tovar, B. Lucas-granados, M. J. Muñoz-Portero and J. García-Antón, *Chem. Eng. J.*, 2018, **350**, 1114–1124.
64 T. Dong, Z. Zheng, J. H. K. Man and I. M. C. Lo, *Chem. Eng. J.*, 2024, **499**, 155840.
65 M. Jia, Q. Liu, W. Xiong, Z. Yang, C. Zhang, D. Wang, Y. Xiang, H. Peng, J. Tong, J. Cao and H. Xu, *Appl. Catal., B*, 2022, **310**, 121344.
66 S. Seenivasan, S. Adhikari and D. Kim, *Chem. Eng. J.*, 2021, **422**, 130137.
67 G. Li, Z. Lian, W. Wang, D. Zhang and H. Li, *Nano Energy*, 2016, **19**, 446–454.
68 P. Mane, I. V. Bagal, H. Bae, M. A. Kulkarni, A. Abdullah, S. Ryu and J. Ha, *J. Electroanal. Chem.*, 2022, **922**, 116729.
69 J. Huang, T. Lin, L. Lin, G. Ma, Z. Zhang, S. Handschuh-Wang, A. Meng, P. Han and B. He, *ACS Appl. Energy Mater.*, 2024, **7**, 10710–10720.
70 J. Li, X. Li, S. Yu, S. Gao, Y. Zhang, Y. Li, C. Wang and Q. Wang, *Chin. Chem. Lett.*, 2023, **34**, 107417.
71 S. He, D. Xie, B. Wang, M. Zhu and S. Hu, *J. Colloid Interface Sci.*, 2023, **650**, 1993–2002.
72 X. Z. Li and H. S. Liu, *Environ. Sci. Technol.*, 2005, **39**, 4614–4620.
73 H. Feng, Y. Liang, K. Guo, N. Li, D. Shen, Y. Cong, Y. Zhou, Y. Wang, M. Wang and Y. Long, *Water Res.*, 2016, **102**, 428–435.
74 Z. Zheng, J. H. K. Man and I. M. C. Lo, *Environ. Sci. Technol.*, 2022, **56**, 16156–16166.
75 O. Samuel, M. H. D. Othman, R. Kamaludin, O. Sinsamphanh, H. Abdullah, M. H. Puteh and T. A. Kurniawan, *Ceram. Int.*, 2022, **48**, 5845–5875.
76 F. Zhao, W. Li, Y. Song, Y. Fu, X. Liu, C. Ma, G. Wang, X. Dong and H. Ma, *Appl. Mater. Today*, 2022, **26**, 101390.
77 Y. Zhou, X. Fan, G. Zhang and W. Dong, *Chem. Eng. J.*, 2019, **356**, 1003–1013.
78 X. Wang, G. Liu, J. Liu, G. Ren and P. Wang, *Chem. Eng. J.*, 2024, **495**, 153170.
79 Y. Peng and S. C. E. Tsang, *Nano Today*, 2018, **18**, 15–34.
80 R. A. Rather, A. Mehta, Y. Lu, M. Valant, M. Fang and W. Liu, *Int. J. Hydrogen Energy*, 2021, **46**, 21866–21888.
81 J. Yang, N. Sun, Z. Zhang, J. Bian, Y. Qu, Z. Li, M. Xie, W. Han and L. Jing, *ACS Appl. Mater. Interfaces*, 2020, **12**, 28264–28272.
82 H. Wu, Z. Hu, R. Liang, X. Zhang, M. Zhou and O. A. Arotiba, *J. Hazard. Mater.*, 2023, **456**, 131696.
83 H. Wang, S. Wang, M. T. Oo, Y. Yang, J. Zhou, M. Huang and R. Zhang, *J. Colloid Interface Sci.*, 2023, **646**, 687–694.
84 Y. Wang, J. Wu, Y. Yan, L. Li, P. Lu, J. Guan, N. Lu and X. Yuan, *Chem. Eng. J.*, 2021, **403**, 126313.
85 F. Khodabandeloo, M. Sheydaei, P. Moharramkhani, M. Masteri-Farahani and A. Khataee, *Chemosphere*, 2023, **330**, 138766.
86 J. Liu, J. Li, M. Shao and M. Wei, *J. Mater. Chem. A*, 2019, **7**, 6327–6336.
87 K. Guima, L. E. Gomes, J. Alves Fernandes, H. Wender and C. A. Martins, *ACS Appl. Mater. Interfaces*, 2020, **12**, 54563–54572.
88 H. Wu, J. Jing, S. Li, S. Li, J. Liu, R. Liang, Y. Zhang, Z. Xia and M. Zhou, *Appl. Catal. B-Environ. Energy*, 2025, **360**, 124517.
89 R. A. Rather and I. M. C. Lo, *Water Res.*, 2020, **168**, 115166.
90 H. Wu, Z. Hu, R. Liang, O. V. Nkwachukwu, O. A. Arotiba and M. Zhou, *Appl. Catal., B*, 2023, **321**, 122053.
91 G. Zhang, Z. Zhang, D. Xia, Y. Qu and W. Wang, *J. Hazard. Mater.*, 2020, **392**, 122292.
92 Z. Zheng and I. M. C. Lo, *Appl. Catal., B*, 2021, **299**, 120636.
93 K. Zuo, S. Garcia-Segura, G. A. Cerrón-Calle, F. Chen, X. Tian, X. Wang, X. Huang, H. Wang, P. J. J. Alvarez, J. Lou, M. Elimelech and Q. Li, *Nat. Rev. Mater.*, 2023, **8**, 472–490.
94 C. Liu, N. Zhang, Y. Li, R. Fan, W. Wang, J. Feng, C. Liu, J. Wang, W. Hao, Z. Li and Z. Zou, *Nat. Commun.*, 2023, **14**, 4266.
95 X. Li, J. Wan, Y. Ma, Y. Wang and X. Li, *Chem. Eng. J.*, 2021, **404**, 127054.
96 R. Gao, Z. Gao, N. T. Nguyen, J. Chen, X. Liu, L. Wang and L. Wu, *Nat. Sustainability*, 2025, 1–10, DOI: **10.1038/s41893-025-01530-y**.
97 J. Zhang, G. Zhang, H. Lan, H. Liu and J. Qu, *Chem. Eng. J.*, 2022, **428**, 130373.
98 M. S. Koo, X. Chen, K. Cho, T. An and W. Choi, *Environ. Sci. Technol.*, 2019, **53**, 9926–9936.
99 Y. Zhang, J. Li, J. Bai, L. Li, S. Chen, T. Zhou, J. Wang, L. Xia, Q. Xu and B. Zhou, *Environ. Sci. Technol.*, 2019, **53**, 6945–6953.
100 T. Le Bahers and K. Takanabe, *J. Photochem. Photobiol., C*, 2019, **40**, 212–233.
101 A. B. Murphy, *Sol. Energy Mater. Sol. Cells*, 2007, **91**, 1326–1337.
102 C. M. Tian, W. W. Li, Y. M. Lin, Z. Z. Yang, L. Wang, Y. G. Du, H. Y. Xiao, L. Qiao, J. Y. Zhang, L. Chen, D. Qi, J. L. MacManus-Driscoll and K. H. L. Zhang, *J. Phys. Chem. C*, 2020, **124**, 12548–12558.
103 Z. Wang, X. Zong, Y. Gao, J. Han, Z. Xu, Z. Li, C. Ding, S. Wang and C. Li, *ACS Appl. Mater. Interfaces*, 2017, **9**, 30696–30702.
104 B. Lei, D. Xu, B. Wei, T. Xie, C. Xiao, W. Jin and L. Xu, *ACS Appl. Mater. Interfaces*, 2021, **13**, 4785–4795.
105 Q. Zeng, J. Li, L. Li, J. Bai, L. Xia and B. Zhou, *Appl. Catal., B*, 2017, **217**, 21–29.
106 X. Li, M. Kan, T. Wang, Z. Qin, T. Zhang, X. Qian, Y. Kuwahara, K. Mori, H. Yamashita and Y. Zhao, *Appl. Catal., B*, 2021, **296**, 120387.
107 K. Feng, Y. Lin, J. Guo, Z. Ye, Y. Zhang, Q. Ma, Y. Shao, K. Chen, J. Zhuang, D. Lin and T. Lin, *J. Hazard. Mater.*, 2020, **393**, 122488.
108 Y. Tang, Z. Zheng, X. Sun, X. Li and L. Li, *Chem. Eng. J.*, 2019, **368**, 448–458.
109 B. A. Koiki, B. O. Orimolade, B. N. Zwane, O. V. Nkwachukwu, C. Muzenda, D. Nkosi and O. A. Arotiba, *Chemosphere*, 2021, **266**, 129231.
110 Y. Jin, P. Zhang, X. Wang, H. Ma and Y. Zhang, *Chem. Eng. J.*, 2024, **491**, 152168.

111 Y. Yang, H. Chen, X. Zou, X. Shi, W. Liu, L. Feng, G. Suo, X. Hou, X. Ye, L. Zhang, C. Sun, H. Li, C. Wang and Z. Chen, *ACS Appl. Mater. Interfaces*, 2020, **12**, 24845–24854.
112 H. L. Tan, R. Amal and Y. H. Ng, *J. Mater. Chem. A*, 2017, **5**, 16498–16521.
113 H. Zhang, J. H. Park, W. J. Byun, M. H. Song and J. S. Lee, *Chem. Sci.*, 2019, **10**, 10436–10444.
114 Q. Zeng, J. Li, L. Li, J. Bai, L. Xia and B. Zhou, *Appl. Catal., B*, 2017, **217**, 21–29.
115 L. Chen, J. Ren and Z. Yuan, *Adv. Energy Mater.*, 2023, 2203720.
116 W. Yang and Y. Wang, *Appl. Catal., B*, 2021, **282**, 119574.
117 J. Liu, J. Li, Y. Li, J. Guo, S. Xu, R. Zhang and M. Shao, *Appl. Catal., B*, 2020, **278**, 119268.
118 F. Liang and Y. Zhu, *Appl. Catal., B*, 2016, **180**, 324–329.
119 T. Su, Y. Gong, X. Cui, X. Wang, Y. Zhang and H. Yu, *Chem. Eng. J.*, 2024, **497**, 155036.
120 L. Xia, F. Chen, J. Li, S. Chen, J. Bai, T. Zhou, L. Li, Q. Xu and B. Zhou, *J. Hazard. Mater.*, 2020, **389**, 122140.
121 Z. Feng, Q. Tian, Q. Yang, Y. Zhou, H. Zhao and G. Zhao, *Appl. Catal., B*, 2021, **286**, 119908.
122 Y. Guo, J. Long, J. Huang, G. Yu and Y. Wang, *Water Res.*, 2022, **215**, 118275.
123 Y. Lei, Y. Yu, X. Lei, X. Liang, S. Cheng, G. Ouyang and X. Yang, *Environ. Sci. Technol.*, 2023, **57**, 5433–5444.
124 P. J. Mafa, M. E. Malefane, F. Opoku, B. B. Mamba and A. T. Kuvarega, *Chem. Eng. J.*, 2023, **464**, 142462.
125 P. Zhang, Y. Yang, X. Duan, Y. Liu and S. Wang, *ACS Catal.*, 2021, **11**, 11129–11159.
126 W. Yu, C. Feng, R. Li, B. Zhang and Y. Li, *Chin. J. Catal.*, 2025, **68**, 51–82.
127 M. Hillenbrand, C. Helbig and R. Marschall, *Energy Environ. Sci.*, 2024, **17**, 2369–2380.
128 J. Fu, Z. Fan, M. Nakabayashi, H. Ju, N. Pastukhova, Y. Xiao, C. Feng, N. Shibata, K. Domen and Y. Li, *Nat. Commun.*, 2022, **13**, 729.
129 X. Zhan, T. Lei, L. Wang, H. Zhang, D. Ou, M. Yang, M. Guo, Y. Luo, L. Tang, H. Yang, W. Yang and H. Hou, *J. Photochem. Photobiol., A*, 2024, **451**, 115538.
130 S. Li, J. Chen, S. Hu, H. Wang, W. Jiang and X. Chen, *Chem. Eng. J.*, 2020, **402**, 126165.
131 Z. Hu, H. Wu, S. Li, C. Zhang, R. Liang and M. Zhou, *Chem. Eng. J.*, 2024, **498**, 155308.